The Astrophysical Journal, 850:96 (17pp), 2017 November 20 https://doi.org/10.3847/1538-4357/aa960c
© 2017. The American Astronomical Society. All rights reserved.

The Geometry of the Sagittarius Stream from Pan-STARRS1 3π RR Lyrae

Nina Hernitschek[1,2], Branimir Sesar[2], Hans-Walter Rix[2], Vasily Belokurov[3], David Martinez-Delgado[4], Nicolas F. Martin[2,5], Nick Kaiser[6], Klaus Hodapp[6], Kenneth C. Chambers[6], Richard Wainscoat[6], Eugene Magnier[6], Rolf-Peter Kudritzki[6], Nigel Metcalfe[7], and Peter W. Draper[7]

[1] Division of Physics, Mathematics and Astronomy, Caltech, Pasadena, CA 91125, USA; ninah@astro.caltech.edu
[2] Max-Planck-Institut für Astronomie, Königstuhl 17, D-69117 Heidelberg, Germany
[3] Institute of Astronomy, University of Cambridge, Madingley Road, Cambridge CB3 0HA, UK
[4] Astronomisches Rechen-Institut, Zentrum für Astronomie der Universität Heidelberg, Mönchhofstr. 12-14, D-69120 Heidelberg, Germany
[5] Observatoire astronomique de Strasbourg, Université de Strasbourg, CNRS, UMR 7550, 11 rue de l'Université, F-6700 Strasbourg, France
[6] Institute for Astronomy, University of Hawaii at Manoa, Honolulu, HI 96822, USA
[7] Department of Physics, University of Durham, South Road, Durham DH1 3LE, UK

Received 2017 August 11; revised 2017 October 23; accepted 2017 October 23; published 2017 November 21

Abstract

We present a comprehensive and precise description of the Sagittarius (Sgr) stellar stream's 3D geometry as traced by its old stellar population. This analysis draws on the sample of ~44,000 RR Lyrae (RRab) stars from the Pan-STARRS1 (PS1) 3π survey, which is ~80% complete and ~90% pure within 80 kpc, and extends to $\gtrsim$120 kpc with a distance precision of ~3%. A projection of RR Lyrae stars within $|\tilde{B}|_\odot < 9°$ of the Sgr stream's orbital plane reveals the morphology of both the leading and the trailing arms at very high contrast across much of the sky. In particular, the map traces the stream near-contiguously through the distant apocenters. We fit a simple model for the mean distance and line-of-sight depth of the Sgr stream as a function of the orbital plane angle $\tilde{\Lambda}_\odot$, along with a power-law background model for the field stars. This modeling results in estimates of the mean stream distance precise to ~1% and it resolves the stream's line-of-sight depth. These improved geometric constraints can serve as new constraints for dynamical stream models.

Key words: galaxies: dwarf – stars: variables: RR Lyrae

Supporting material: machine-readable table

1. Introduction

Stellar streams around galaxies, and in particular around the Milky Way, are of great interest because their orbits are sensitive tracers of a galaxy's formation history and gravitational potential (e.g., Eyre & Binney 2009; Law & Majewski 2010; Newberg et al. 2010; Sanders & Binney 2013). In the Milky Way, the Sagittarius (Sgr) stream is the dominant tidal stellar stream of the Galactic stellar halo, and its extent has been traced around much of the sky. The stream shows two pronounced tidal tails, each extending ~180° and reaching Galactocentric distances from 20 to more than 100 kpc, also referred to as "leading arm" and "trailing arm" (Majewski et al. 2003).

Stellar streams are sets of stars on similar orbits and therefore lend themselves to constraining the dynamical mass within their orbit. The distribution of the Sgr stream's stars can therefore serve as a probe of the Galactic mass profile and shape, including the dark matter halo. This is best done with six-dimensional phase-space information available for the stars, as has been shown for relatively nearby streams such as GD-1 (Koposov et al. 2010; Bovy et al. 2016) and Ophiuchus (Sesar et al. 2016).

Since its discovery by Ibata et al. (1994), several studies on sections of the Sagittarius stream have been carried out. The first modeling attempt was done by Johnston et al. (1995), but it found that the progenitor, the Sagittarius dwarf galaxy, disrupted after only two orbits, while observations show the completion of about 10 orbits. As a solution to the problem, Ibata & Lewis (1998) concluded from an extensive numerical study that the Sagittarius dwarf galaxy must have a stiff and extended dark matter halo if it still has about 25% of its initial mass and is still bound today.

Early pencil-beam surveys before the era of large-scale surveys were used by Mateo et al. (1998) and Martínez-Delgado et al. (2001, 2003), reporting detections of tidal debris in the northern stream of the Sagittarius dwarf galaxy and leading to the publication of one of the first models of the Sagittarius stream to be in good agreement with the observations (Martínez-Delgado et al. 2003). Since the first detailed mapping by Majewski et al. (2003), there have been quite a number of attempts to map and trace the Sgr stream over larger fractions of its extent, building at least in part, e.g., on the seminal work by Majewski et al. (2003). Such work was carried out by Niederste-Ostholt et al. (2010), who traced the Sgr stream out to $D \sim 50$ kpc using main-sequence, red giant, and horizontal branch stars from the Sloan Digital Sky Survey (SDSS) as well as M giants from the Two Micron All-sky Survey (2MASS), by Koposov et al. (2012), who used main-sequence turn-off (MSTO) stars to measure the stream's distance gradients in the range $\tilde{\Lambda}_\odot = 90°$–$130°$ in the southern Galactic hemisphere, and by Slater et al. (2013) using color-selected MSTO stars from the Pan-STARRS1 survey to present a panoramic view of the Sgr tidal stream in the southern Galactic hemisphere spanning $\tilde{\Lambda}_\odot = 70°$–$130°$.

Wide-area surveys of the Galactic halo, employing RR Lyrae as tracers, have already been used in the past: Vivas et al. (2001) carried out a study on 148 RR Lyrae within the first 100 deg^2 of the Quasar Equatorial Survey Team (QUEST) RR Lyrae survey, and after publishing a catalog (Vivas et al. 2004) they continued using QUEST for finding substructure near the Virgo overdensity (Vivas et al. 2008). Duffau et al. (2014) (with Vivas) have extended the sample and found various velocity groups from QUEST and QUEST–La Silla (Zinn et al. 2014). Sesar et al. (2012) found two new halo velocity groups using RR Lyrae from

the Palomar Transient Factory (PTF) survey; Sesar et al. (2013) used a sample of ∼5000 RR Lyrae over ∼8000 deg^2 of sky from the the Lincoln Near-Earth Asteroid Research asteroid survey (LINEAR) to analyze the Galactic stellar halo profile for heliocentric distances between 5 kpc and 30 kpc. Drake et al. (2014) produced a catalog of RR Lyrae and other periodic variables from the Catalina Surveys Data Release-1 (CSDR1).

A number of these attempts have been able to map parts of the Sagittarius stream. An extensive map was made by Drake et al. (2013, 2014), which confirms the presence of a halo structure that appears as part of the Sagittarius tidal stream but is inconsistent with *N*-body simulations of that stream such as the model of Law & Majewski (2010). Recently, this feature was confirmed by Belokurov et al. (2014) based on M giants.

In more recent work, Belokurov et al. (2014) have demonstrated that the trailing arm of the Sgr stream can be traced out to its apocenter at ∼100 kpc. They also give a fit of the stream's leading arm to its apocenter at ∼50 kpc. The extent of the Sgr stream has therefore only recently become fully apparent, spanning an unparalleled range of distances when compared to other stellar tidal streams in the Milky Way.

In contrast to the aforementioned partial mapping of the Sgr stream, showing the stream only piecewise mapped by tracers from different surveys and often relying on different kinds of sources as tracers, the data we have at hand—RR Lyrae stars from Pan-STARRS1—enable us to trace the complete angular extent of the Sgr stream as well as to look even at the outskirts of the stream.

There have also been attempts to model the Sagittarius tidal stream (e.g., Law & Majewski 2005; Peñarrubia et al. 2010; Gibbons et al. 2014), which has complex geometry and incomplete (so far) phase-space information.

Helmi (2004a, 2004b) claim that the trailing arm is too young to be a probe of the dark matter profile, whereas the leading arm, being slightly older, provides direct evidence for the prolate shape of the dark matter halo. Helmi (2004a, 2004b) have used numerical simulations of the Sgr stream to probe the profile of the Milky Way's dark matter halo. They find that the data available for the stream are consistent with a Galactic dark matter halo that could be either oblate or prolate, with a ratio of minor to major density axes that can be as low as 0.6 within the region probed by the Sgr stream. In agreement with Martínez-Delgado et al. (2003), they state that the dark matter halo should thus not be assumed to be nearly spherical.

The modeling efforts have also included *N*-body simulations constrained by observational data (e.g., Fellhauer et al. 2006; Law & Majewski 2010; Peñarrubia et al. 2010; Dierickx & Loeb 2017). Consistent 3D stream constraints from a single survey, as we set out to provide here, aid the comparison to models of the Sgr stream, usually based on *N*-body simulation (e.g., Law & Majewski 2010; Dierickx & Loeb 2017).

The main aim of this paper is to map the geometry (in particular the distance) of the Sgr stream more precisely, accurately, and comprehensively than before, using exclusively RR Lyrae (RRL) stars from a single survey to trace the stream's old stellar population. For our analysis, we use the RRab sample of Sesar et al. (2017c), which covers 3/4 of the sky, is rather pure, and has precise distances (to 3%). It was generated from data of the Pan-STARRS1 survey (PS1) (Kaiser et al. 2010), using structure functions and a machine-learning algorithm by Hernitschek et al. (2016) and a subsequent multiband light-curve fitting and another machine-learning algorithm as described in Sesar et al. (2017c).

This provides us with an RRL map of the old Galactic stellar halo that is of high enough contrast to fit the Sgr stream geometry directly by a density model: its distance and line-of-sight depth as a function of angle in its orbital plane. In particular, we can derive precise apocenter positions of both the leading and trailing arms and thus the Galactocentric orbital precession of the stream.

The structure of the paper is as follows: in Section 2 we describe the PS1 survey and the RRL sample derived from it; in Section 3 we describe and apply the distance distribution model for the Sgr stream that we fit to these data; in Section 4 we present and discuss our results obtained from evaluating the fit, describe our findings regarding geometrical properties of the stream, and compare them to earlier work; we conclude with a discussion in Section 5 and a summary in Section 6.

This work is part of a series of papers exploring the identification and astrophysical exploitation of RRL stars in the PS1 survey. The basic approach for applying multiband structure functions to PS1 3π light curves, and subsequently using a classifier evaluating variability and color information to select RR Lyrae and QSO candidates, has been laid out in Hernitschek et al. (2016), with results from the preliminary PS1 3π version, PV2. We then applied multiband fitting of the period to all these RRL candidates (Sesar et al. 2017c), using light curves from the final PS1 3π version, PV3. The quality and plausibility of these fits aided in the classification, increasing the purity of the sample and leading to precise distance estimates for the sample of RRab stars. Sesar et al. (2017b) show new detections within the Sgr stream, made using the RRab sample without further fitting or modeling; in particular, they show the detection of spatially distinct "spur" and clump features reaching out to more than 100 kpc on top of the apocenters of the Sgr stream, which is in good agreement with recent dynamical models (Gibbons et al. 2014; Fardal et al. 2015; Dierickx & Loeb 2017).

2. RR Lyrae Stars from the PS1 Survey

Our analysis is based on a sample of highly likely RRab stars, as selected by Sesar et al. (2017c) from the Pan-STARRS1 3π survey. In this section, we describe the pertinent properties of the PS1 3π survey and its obtained light curves, recapitulate briefly the process of selecting the likely RRab, as laid out in Sesar et al. (2017c), and briefly characterize the obtained candidate sample.

The Pan-STARRS1 (PS1) survey (Kaiser et al. 2010) is collecting multiepoch, multicolor observations via a number of surveys, among which the PS1 3π survey (Stubbs et al. 2010; Tonry et al. 2012; Chambers et al. 2016) is currently the largest. It has observed the entire sky north of decl. $-30°$ in five filter bands ($g_{\rm P1}$, $r_{\rm P1}$, $i_{\rm P1}$, $z_{\rm P1}$, $y_{\rm P1}$) with 5σ single-epoch depths of 22.0, 21.8, 21.5, 20.9, and 19.7 magnitudes in $g_{\rm P1}$, $r_{\rm P1}$, $i_{\rm P1}$, $z_{\rm P1}$, and $y_{\rm P1}$, respectively (Chambers et al. 2016).

For more than 1.1×10^9 PS1 3π PV3 sources, we constructed a set of data features for source classification: the sources' mean magnitudes in various bands, as well as multiband variability features such as a simple χ^2-related variability measure $\hat{\chi}^2$, and multiband structure function parameters, (ω_r, τ), describing the characteristic amplitude and timescale of variability (Hernitschek et al. 2016). Based on these features, including a multiband light-curve fit resulting in period estimates, a machine-learned classifier, trained on PS1 3π sources within SDSS S82, then selects plausible RRL candidates (Sesar et al. 2017c). Their distances were calculated based on a newly derived period–luminosity relation for the optical/near-infrared PS1

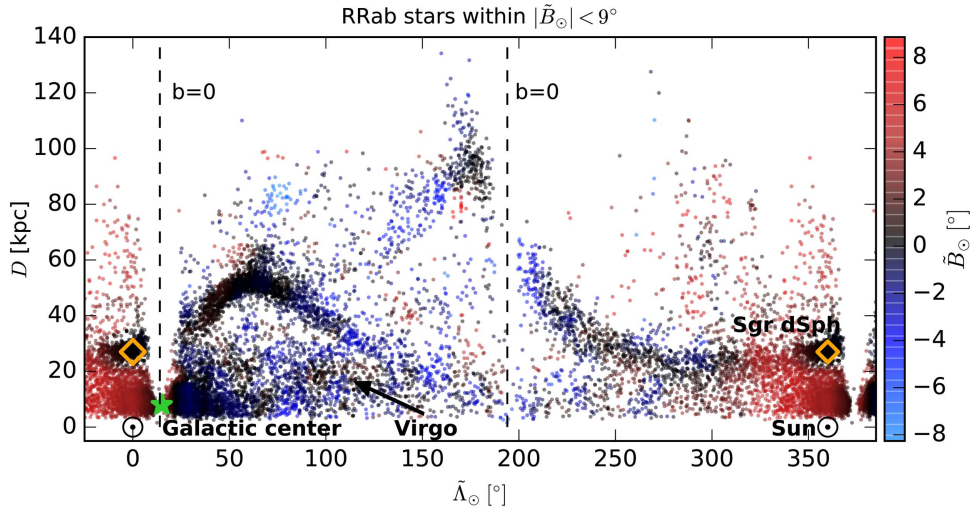

Figure 1. RRab stars within $|\tilde{B}_\odot| < 9°$ as obtained after fitting of the period (Sesar et al. 2017c). The Sgr stream is clearly visible up to ∼130 kpc. The color indicates the median angular distance $\tilde{B}_\odot$ of a 5° × 5 kpc bin (in $\tilde{\Lambda}_\odot$ and D coordinates) from the Sgr orbital plane $\tilde{B}_\odot = 0°$. This was chosen due to the high source density in some regions. In this figure, the angular coordinate $\tilde{\Lambda}_\odot$ runs from −20° to 380° with repeated data points for $\tilde{\Lambda}_\odot < 0°$ and $\tilde{\Lambda}_\odot > 360°$, to better show the distribution near $\tilde{\Lambda}_\odot \sim 0°$. The locations of the Sun, Galactic anticenter, Sgr dSph, and the Virgo overdensity (Vivas et al. 2001; Newberg et al. 2003; Jurić et al. 2008) are indicated. The dashed line marks the position of the Galactic plane. The centroid for Sgr dSph was taken from Karachentsev et al. (2004). The Cetus stream should cross the Sgr stream at $\tilde{\Lambda}_\odot \sim 270°$, $\tilde{B}_\odot \sim 1°$ (Newberg et al. 2009). Evidence from our data is marginal.

bands, because the majority of the PS1 sources lack metallicities. The complete methodology on how to derive the distances and verify their precision is given in Sesar et al. (2017c).

Overall, this highly effective identification of RR Lyrae stars has resulted in the widest (3/4 of the sky) and deepest (reaching >120 kpc) sample of those stars to date. The RRab sample from Sesar et al. (2017c) was selected uniformly from the set of sources in the PS1 3π survey in the area and range of apparent magnitude available for this survey. Sesar et al. (2017c) have shown that the selection completeness and purity for sources at high Galactic latitudes ($|b| > 15°$) are approximately uniform over a wide range of apparent magnitude up to a flux-averaged r-band magnitude of 20 mag, maintaining a sample completeness for the RRab stars of ∼80% and a purity of ∼90% within 80 kpc (see their Figure 11).

We thus explicitly refer to high-latitude completeness on PS1 3π overlapping with SDSS Stripe 82 (Sesar et al. 2017c), but we have no reason to believe that the purity and completeness vary strongly across high-latitude areas. A detailed map of the purity and completeness including not only their distance but their spatial distribution would require that we have "ground truth" (i.e., knowledge about the true type of star for every source) in all directions, which of course is not available. For the definition of completeness and purity, we refer to Sesar et al. (2017c), where the completeness is defined as the fraction of recovered RR Lyrae stars on a test area (e.g., SDSS Stripe 82), and the purity is defined as the fraction of true RR Lyrae stars in the selected sample of RR Lyrae candidates.

There are 44,403 likely RRab stars in this PS1 sample with distance estimates that are precise to 3%. In the further analysis, we refer to this sample (Hernitschek et al. 2016; Sesar et al. 2017c) as "RRab stars."

While the sample covers the entire sky above decl. −30°, we focus on stars near the orbital plane of the Sgr stream. We use the heliocentric Sagittarius coordinates ($\tilde{\Lambda}_\odot$, $\tilde{B}_\odot$) as defined by Belokurov et al. (2014), where the equator $\tilde{B}_\odot = 0°$ is aligned with the plane of the stream. We restrict our subsequent analysis to RRab from our sample that lie within $|\tilde{B}_\odot| < 9°$ as also seen in the plots by Belokurov et al. (2014), resulting in ∼15,000 stars. This sample is plotted in Figure 1 in the ($\tilde{\Lambda}_\odot$, D) plane of longitudinal coordinates $\tilde{\Lambda}_\odot$ and heliocentric distances D, with the angular distance to the Sgr plane $\tilde{B}_\odot$ indicated by color coding. A table for these stars within $|\tilde{B}_\odot| < -9°$ is given in the Appendix, Table 1. A machine-readable version of this table is available in the electronic version of the Journal.

3. A Simple Model to Characterize the Geometry of the Sgr Stream

We aim at a simple quantitative description of the Sgr stream, by providing the mean distance and line-of-sight (l.o.s.) depth of presumed member stars as a function of angle in the orbital plane. We only consider stars within $|\tilde{B}_\odot| < 9°$, and marginalize over their distribution perpendicular to the orbital plane, resulting in a set of distances as a function of $\tilde{\Lambda}_\odot$. In practice, the overall distance distribution $p_{\rm RRL}(D)$ toward any $\tilde{\Lambda}_\odot$ is modeled as the superposition of a "stream" and a "halo" component. For each $\tilde{\Lambda}_\odot$ bin, the halo is modeled as a power-law $\rho_{\rm halo}$ in Galactic coordinates, describing the background of field stars. The heliocentric distance distribution of stream stars is modeled as a Gaussian, characterized by $D_{\rm sgr}$ and the l.o.s. depth, $\sigma_{\rm sgr}$:

$$\begin{aligned} p_{\rm RRL}(\mathcal{D}|\boldsymbol{\theta}) &= p_{\rm halo}(\mathcal{D}|\boldsymbol{\theta}) + p_{\rm stream}(\mathcal{D}|\boldsymbol{\theta}) \\ &= (1 - f_{\rm sgr}) \times \hat{\rho}_{\rm halo}(l, b, D, q, n) \\ &\quad + f_{\rm sgr} \times \hat{\rho}_{\rm sgr}(l, b, D, D_{\rm sgr}, \sigma_{\rm sgr}), \end{aligned} \tag{1}$$

where

$$\hat{\rho}_{\rm halo}(l, b, D, q, n) \equiv \frac{\rho_{\rm halo}(l, b, D, q, n)}{\int_{D_{\rm min}}^{D_{\rm max}} \rho_{\rm halo}(l, b, D, q, n) {\rm d}D}, \tag{2}$$

with an analogous definition of $\hat{\rho}_{\rm sgr}$. The data set is given as $\mathcal{D} = (D, \delta D, l, b)$. The parameters are $\boldsymbol{\theta} = (f_{\rm sgr}, D_{\rm sgr}, \sigma_{\rm sgr}, n)$, composed of the fraction of stars $f_{\rm sgr}$ that lie in the Sgr stream at the given $\tilde{\Lambda}_\odot$ slice, the heliocentric distance of the stream

$D_{\rm sgr}$, its l.o.s. depth $\sigma_{\rm sgr}$, and the power-law index n of the halo model. $D_{\rm min}$ and $D_{\rm max}$ are the minimum and maximum D we consider in each $\tilde{\Lambda}_\odot$ slice.

We adopt a simple power-law halo model $\rho_{\rm halo}$ (Sesar et al. 2013) to describe the "background" of field stars in the direction of (l, b):

$$\rho_{\rm halo}(X, Y, Z) = \rho_{\odot\rm RRL}(R_\odot/r_q)^n \tag{3}$$

with

$$\begin{aligned} X &= R_\odot - D\cos l\cos b \\ Y &= -D\sin l\cos b \\ Z &= D\sin b \\ r_q &= \sqrt{X^2 + Y^2 + (Z/q)^2}. \end{aligned}$$

Sesar et al. (2013) also give the halo parameters

$$\begin{aligned} n &= 2.62 \\ R_\odot &= 8.0\ \text{kpc} \\ q &= 0.71 \\ \rho_{\odot\ \rm RRL} &= 4.5\ \text{kpc}^{-3}. \end{aligned}$$

Here, $\rho_{\odot\rm RRL}$ is the number density of RR Lyrae at the position of the Sun; q gives the halo flattening along the Z direction. In our analysis, all "background halo" parameters except the fitting parameter n are kept fixed.

The stream is modeled as a normal distribution centered on $D_{\rm sgr}$ and with variance $\sigma_{\rm sgr}$ as follows. It is defined in Galactic coordinates (l, b) and Galactocentric distance R, where R is given as a function of the heliocentric distances D, $D_{\rm sgr}$, and distance uncertainty δD, as follows:

$$\begin{aligned} &\rho_{\rm sgr}(l, b, D, \delta D, D_{\rm sgr}, \sigma_{\rm sgr}) \\ &= \frac{1}{\sqrt{2\pi(\sigma_{\rm sgr}^2 + \delta D^2)}} \exp\left(-\frac{(R(D) - R(D_{\rm sgr}))^2}{2(\sigma_{\rm sgr}^2 + \delta D^2)}\right) D^2. \end{aligned} \tag{4}$$

For the distance uncertainties of RRab stars, we adopt a δD of 3% according to Sesar et al. (2017c).

3.1. Fitting the Sgr Model

For fitting this model, the sample of RRab stars near the Sgr orbital plane is split into bins of $\tilde{\Lambda}_\odot \pm \frac{\Delta\tilde{\Lambda}_\odot}{2}$, each $\Delta\tilde{\Lambda}_\odot = 10°$ wide; the data are not binned in D. In each bin, we fit (independently) the parameters of the stream, $D_{\rm sgr}$ and $\sigma_{\rm sgr}$, along with the halo model parameter n. Whereas it is obvious why the stream-related model parameters should be fitted individually for each $\tilde{\Lambda}_\odot$ bin, the reason for also fitting the halo power-law index n individually is to account for incompleteness of the data. The flattening parameter q is kept fixed at 0.71, because fitting for q did not improve the results for the stream-related model parameters.

To constrain the geometry of the Sgr stream in a probabilistic manner, we calculate the joint posterior probability $p_{\rm RRL}(\boldsymbol{\theta}|\mathcal{D})$ of the parameter set $\boldsymbol{\theta} = (f_{\rm sgr}, D_{\rm sgr}, \sigma_{\rm sgr}, n)$, given the data set $\mathcal{D} = (D, \delta D, l, b)$. The marginal posterior probability of the parameter set $\boldsymbol{\theta}$, $p_{\rm RRL}(\boldsymbol{\theta}|\mathcal{D})$ is related to the marginal likelihood $p_{\rm RRL}(\mathcal{D}|\boldsymbol{\theta})$ through

$$p_{\rm RRL}(\boldsymbol{\theta}|\mathcal{D}) \propto p_{\rm RRL}(\mathcal{D}|\boldsymbol{\theta})p(\boldsymbol{\theta}) \tag{5}$$

where $p(\boldsymbol{\theta})$ is the prior probability of the parameter set.

We evaluate

$$\ln p_{\rm RRL}(\boldsymbol{\theta}|\mathcal{D}) = \sum_i \ln p_{\rm RRL}(\mathcal{D}_i|\boldsymbol{\theta}) + \ln p(\boldsymbol{\theta}) \tag{6}$$

with $p_{\rm RRL}(\mathcal{D}_i|\boldsymbol{\theta})$ given by Equation (1), and i indexes the RRab stars.

We use the following prior probability for the model parameters, $p(\boldsymbol{\theta})$: for $\sigma_{\rm sgr}$, we choose a prior that is uniform in ln, whereas for the other parameters, we adopt uniform priors. Specifically, we adopt

$$\begin{aligned} \ln p(\boldsymbol{\theta}) = &-\ln(\sigma_{\rm sgr}) \\ &+ \text{Uniform}(0.05 \leqslant f_{\rm sgr} < 1) \\ &+ \text{Uniform}(1.7 \leqslant n < 5.0) \\ &+ p(D_{\rm sgr}|\tilde{\Lambda}_\odot). \end{aligned} \tag{7}$$

The prior for $D_{\rm sgr}$ depends on $\tilde{\Lambda}_\odot$, and is uniform within $D_{\rm minprior}(\tilde{\Lambda}_\odot)$, $D_{\rm maxprior}(\tilde{\Lambda}_\odot)$ as indicated in Figure 4 and listed in Tables 2 and 3. Whereas the prior is generally wide, a quite restrictive prior was chosen for $20° \leqslant \tilde{\Lambda}_\odot < 30°$ and $30° \leqslant \tilde{\Lambda}_\odot < 40°$, because the fit otherwise behaves poorly because of the background sources along these l.o.s.

$D_{\rm minprior}$, $D_{\rm maxprior}$ are basically constrained by the minimum and maximum distances in the $\tilde{\Lambda}_\odot$ slice in particular case, but are also defined in order to mask dense regions at short heliocentric distances as well as to separate the leading and trailing arms where both are present at the same l.o.s.

The most probable model given the data is explored using the Affine Invariant Markov Chain Monte Carlo (MCMC) ensemble sampler (Goodman & Weare 2010) as implemented in the `emcee` package (Foreman-Mackey et al. 2013).

The approach was verified with mock data, using a halo component that was sampled from the underlying halo model, superimposed by a mock stream that was inserted as a stellar density sheet; its number density is uniform perpendicular to the l.o.s. and Gaussian along it. The fraction of stream stars with respect to the halo stars, described by $f_{\rm sgr}$, was then successively lowered; i.e., the fit was carried out in the limits of many and few stars in each $\tilde{\Lambda}_\odot$ slice to make sure that reasonable fits can be obtained for densities such as that present for the PS1 3π RR Lyrae candidates, which is ~0.5–1 deg^{-2} for most parts of the sky.

3.2. Fits to Individual $\tilde{\Lambda}_\odot$ Bins

We now illustrate which practical issues are entailed in fitting the model to the data in a $\tilde{\Lambda}_\odot$ bin. Each distance and depth estimate $(D_{\rm sgr}, \sigma_{\rm sgr})$ is obtained by optimizing Equation (6) using an MCMC procedure (Foreman-Mackey et al. 2013). Figures 2 and 3 show fits to individual slices in $\tilde{\Lambda}_\odot$. Figure 2 gives the fit for a 10° wide slice centered on $\tilde{\Lambda}_\odot = 50°$. In this direction, only the leading arm is present. The plot indicates the prior on $D_{\rm sgr}$, in this case, set only by the minimum and maximum distances available from sources in the $\tilde{\Lambda}_\odot$ slice in the particular case. The distribution of the sources is shown, overplotted with the model from the best-fit parameters given as a solid blue line. The transparent blue lines represent samples drawn from the parameter probability density function, illustrating the spread of models; the downturn of the models at small distances below 40 kpc is also a reflection of our sample incompleteness (here at the bright end). In the case in Figure 2, showing $\tilde{\Lambda}_\odot = 55°$, a halo profile much steeper

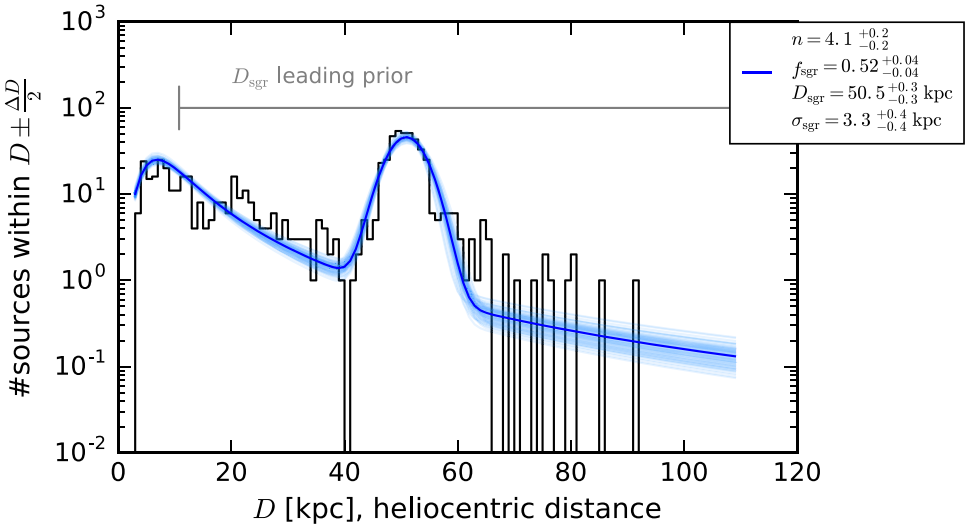

Figure 2. Combined halo and stream fit for a 10° wide slice centered on $\tilde{\Lambda}_\odot = 55°$. In this slice, only the leading arm of the Sgr stream is present. The source distance distribution is shown, overplotted with the model from the best-fit parameters given as the solid blue line. The spread of transparent blue lines gives the spread of models obtained by the MCMC procedure. The best-fit parameters are given along with their 1σ uncertainties. The plot indicates the prior on $D_{\rm sgr}$, set by the minimum and maximum distances available from sources in this $\tilde{\Lambda}_\odot$ slice.

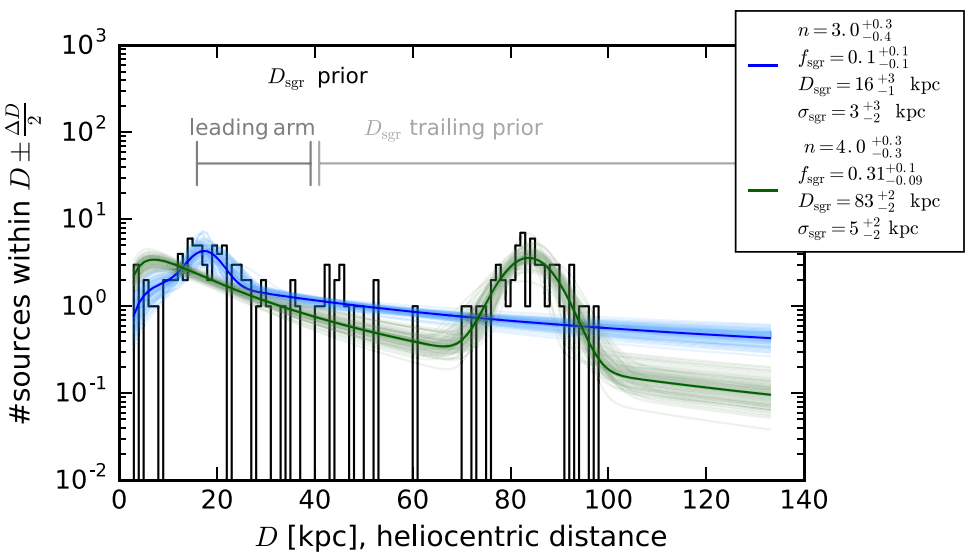

Figure 3. Combined halo and stream fit for a 10° wide slice centered on $\tilde{\Lambda}_\odot = 155°$ where both the leading and trailing arms of the Sgr stream are present. For this plot, the fitting was executed twice, with the different priors indicated. The figure is similar to Figure 2, but shows the influence of a carefully chosen prior to separate the two debris streams. By using distinct priors on $D_{\rm sgr}$, precise estimates of distance and depth of both leading and trailing arms are possible.

than expected from $n = 2.62$ given in the model of Sesar et al. (2013) is obvious; local variations in n presumably reflect simply the halo substructure. The estimate of $D_{\rm sgr}$ and $\sigma_{\rm sgr}$ is clearly seen as being sensible in Figure 2. Here, the variance on the estimated parameters is very small, and the parameters fit well to what one would guess by visual inspection. Even for $\tilde{\Lambda}_\odot$ slices where the fit is poorer (both by visual inspection and by the variance of the distance estimate) a sensible distance estimate, not driven by the priors, is found as we show below.

Figure 3 gives the fit for $\tilde{\Lambda}_\odot = 155°$, where both leading and trailing arms are along the l.o.s. Using distinct priors on $D_{\rm sgr}$ separates the two debris streams and gives precise estimates on distance and depth of both leading and trailing arms (see also Figure 4 around $\tilde{\Lambda}_\odot = 155°$). This illustrates the importance of carefully set priors.

4. Results

The modeling from Section 3 was then applied to the complete sample of RRab stars within $|\tilde{B}_\odot| < 9°$. Figure 4 shows the resulting geometric characterization of the Sgr stream, its fitted distance, and l.o.s. depth (actually $2 \times \sigma_{\rm sgr}$). It is apparent that the estimates of distance and l.o.s. depth trace the stream well all the way out to more than 100 kpc. From this detailed picture of the Sgr stream, many features can be seen in great detail, some of them reported previously. The distances $D_{\rm sgr}$ are shown as black points centered on the $\tilde{\Lambda}_\odot$ slice in each case. The l.o.s. depth $\sigma_{\rm sgr}$ is indicated by black bars. The gray shaded areas mark the priors set on $D_{\rm sgr}$; clearly, in most cases the priors have no significant effect on the probability density function. The fitted parameter values are given in Tables 4 and 5 in the Appendix.

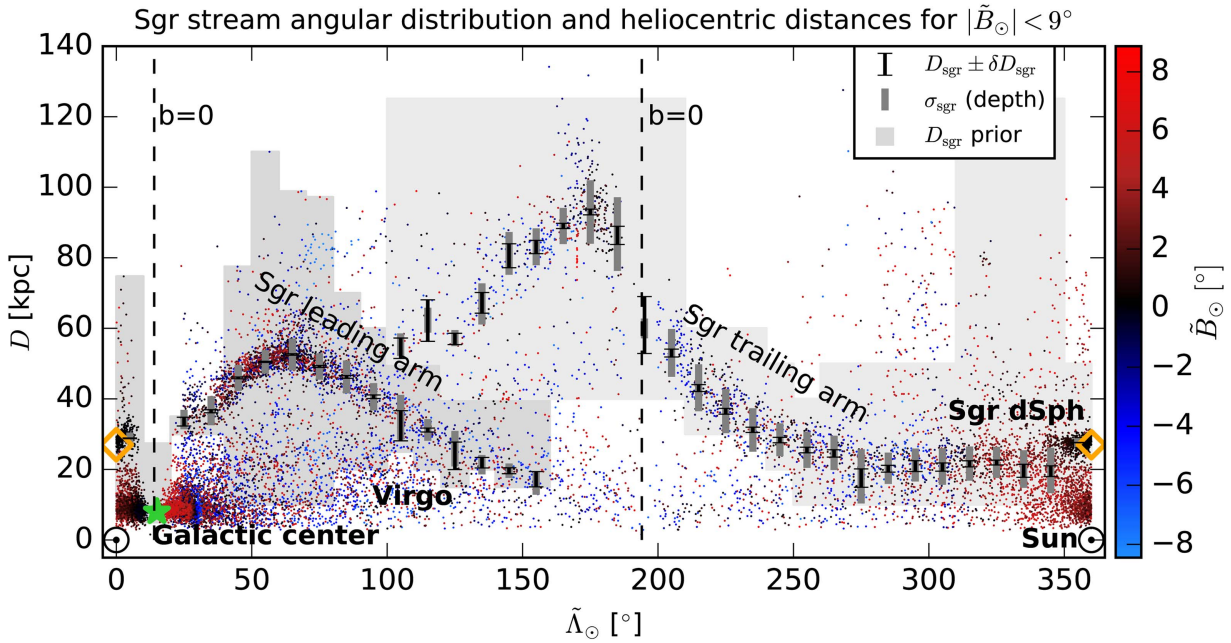

(a)

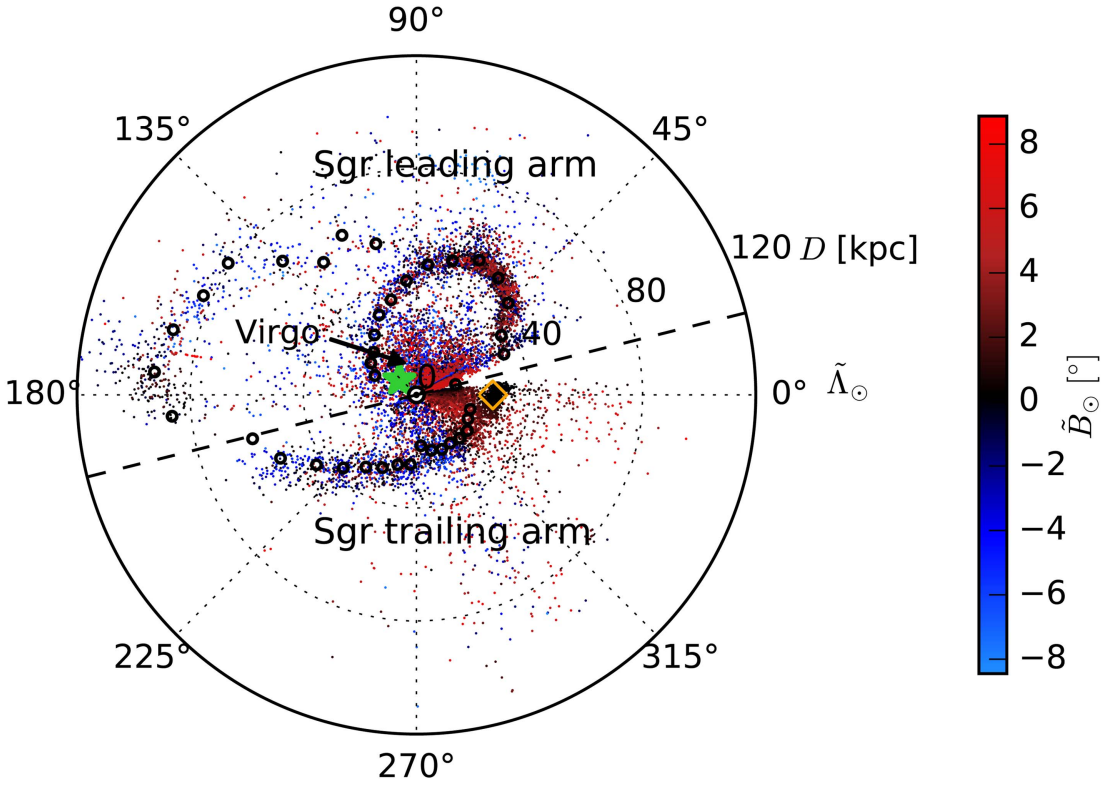

(b)

Figure 4. Source distance distribution is shown with the same color coding and symbols as in Figure 1, overplotted with the fitted extent of the Sgr stream obtained from the method presented in Section 3.1. (a) The extent of the Sgr stream from the RR Lyrae candidates within $\pm 9°$ of the Sagittarius plane, shown in Sagittarius coordinates from Belokurov et al. (2014). The best-fit model, given by $D_{\rm sgr}$, $\sigma_{\rm sgr}$ as obtained for 10° slices in $\tilde{\Lambda}_\odot$, is overplotted. The angular distance of the sources to the Sgr plane $\tilde{B}_\odot = 0°$ is indicated by color coding. The locations of the Sun, Galactic anticenter, Sgr dSph, and the Virgo overdensity are indicated. The dashed line marks the position of the Galactic plane. The black points indicate the center of the $\tilde{\Lambda}_\odot$ slices used to estimate the distance $D_{\rm sgr}$. (b) Projection of the model fit to the stream and distance in cylindrical coordinates centered on the Sun. The same data, symbols, and color coding apply as in (a).

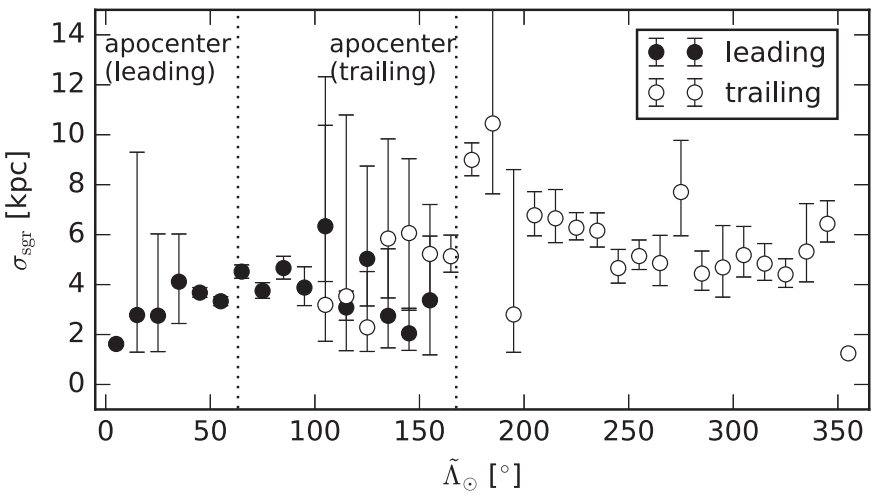

Figure 5. Depth $\sigma_{\rm sgr}$ of the Sagittarius stream from the RRab stars within $\pm 9°$ of the Sagittarius plane. Error bars indicate the range $D_{\rm sgr} \pm \delta D_{\rm sgr}$. A trend in the depth can be seen, reaching a maximum around the apocenter and toward the largest $\tilde{\Lambda}_\odot$ of the leading and trailing arms, respectively. We find the leading arm's apocenter at $\tilde{\Lambda}_\odot^L = 63\overset{\circ}{.}2 \pm 1\overset{\circ}{.}2$, and the trailing arm's apocenter at $\tilde{\Lambda}_\odot^T = 167\overset{\circ}{.}58 \pm 0\overset{\circ}{.}44$. The apocenter positions are indicated here as dashed lines.

Qualitatively the aspects of the Sgr stream shown in Figure 4 can be summarized as follows.

(i) The stream shows clearly distinct leading and trailing arms. The shape and extent look similar to what was found earlier (Majewski et al. 2003; Belokurov et al. 2014), see also Section 5.1.

(ii) The leading arm's apocenter lies between $\tilde{\Lambda}_\odot = 60°$ and 70° where $D_{\rm sgr}$ reaches 48.5–49.6 kpc, and the trailing arm's apocenter is near $\tilde{\Lambda}_\odot \sim 170°$, reaching its largest extent of 92.0 kpc. This agrees with Belokurov et al. (2014), who give the leading arm's apocenter as being located at $\tilde{\Lambda}_\odot = 71\overset{\circ}{.}3 \pm 3\overset{\circ}{.}3$ and the trailing arm's apocenter at $\tilde{\Lambda}_\odot = 170\overset{\circ}{.}5 \pm 1°$. The precise position of the apocenters will be derived in Section 4.3.

(iii) At both the apocenter of the main leading arm ($\tilde{\Lambda}_\odot \sim 70°$) and that of the trailing arm ($\tilde{\Lambda}_\odot \sim 180°$) our RRab map reveals substructure that is readily apparent to the eye and has been further discussed in Sesar et al. (2017b, 2017c): two "clumps" (at $D \sim 60$ and 80 kpc) beyond the leading arm's apocenter, and a "spur" of the trailing arm reaching up to 130 kpc. Such features were previously predicted by dynamical models of the stream (e.g., Gibbons et al. 2014). These new Sgr stream features are discussed in detail in Sesar et al. (2017c).

4.1. The l.o.s. Depth of the Sagittarius Stream

Figure 5 shows the estimated $\sigma_{\rm sgr}$ of the stream (being half the l.o.s. depth) versus $\tilde{\Lambda}_\odot$ for both the leading and trailing arms along with its uncertainty. Figure 5 quantifies what was qualitatively apparent from Figure 4(a): the stream tends to broaden along its orbit from ~1.75 to 6 kpc for the leading arm, reaching even ~10 kpc for the trailing arm. As expected, $\sigma_{\rm sgr}$ and thus the l.o.s. depth are largest close to the apocenters. This is the first systematic determination of the l.o.s. depth, although the uncertainties are still quite large for some parts of the stream. The leading arm's l.o.s. depth rises (and falls) toward (and away) from the apocenter. In contrast, $\sigma_{\rm sgr}$ for the trailing arm remains larger in the range $200° < \tilde{\Lambda}_\odot < 300°$. At least in part, this is presumably because our l.o.s. direction forms a shallower angle with the stream direction than the leading arm. Except toward the apocenters, $\sigma_{\rm sgr}$ also rises toward the "end" (the largest $\tilde{\Lambda}_\odot$) of the respective trailing or leading arm.

In addition to the l.o.s. depth of the Sgr stream, its actual depth would be of great interest. As we know the angle between the normal to the stream and the l.o.s., we could deproject the l.o.s. depth $\sigma_{\rm sgr}$ to get the actual width of the stream.

First, we convert the polar coordinates of the projected ($\tilde{\Lambda}_\odot$, $\tilde{B}_\odot$), as shown in Figure 4, into their Cartesian counterparts ($x_{\rm sgr}$, $y_{\rm sgr}$). We then calculate the deprojected depth $\tilde{\sigma}_{\rm sgr}$ for each bin i in $\tilde{\Lambda}_\odot$ as

$$\tilde{\sigma}_{{\rm sgr},i} = \sigma_{{\rm sgr},i} \cos(\tilde{\Lambda}_{\odot,i} - \alpha_i) \tag{8}$$

with

$$\alpha_i = \tan\left(\frac{y_{{\rm sgr},i+1} - y_{{\rm sgr},i-1}}{x_{{\rm sgr},i+1} - x_{{\rm sgr},i-1}}\right). \tag{9}$$

Equation (9) approximates the tangent in ($x_{{\rm sgr},i}$, $y_{{\rm sgr},i}$) with a line through ($x_{{\rm sgr},i-1}$, $y_{{\rm sgr},i-1}$) and ($x_{{\rm sgr},i+1}$, $y_{{\rm sgr},i+1}$), thus the first and last $\sigma_{\rm sgr}$ of the leading and trailing arms are not deprojected.

The deprojected depths along with their uncertainties are given in Tables 6 and 7 in the Appendix. Figure 6 shows how the l.o.s. and deprojected depth of the Sgr stream vary strongly during the orbital period. The $\tilde{\sigma}_{\rm sgr}$ profile is flatter than the $\sigma_{\rm sgr}$ profile, and as expected, the trailing arm's deprojected depth $\tilde{\sigma}_{\rm sgr}$ is not noticeably boosted, in contrast to $\sigma_{\rm sgr}$, which is. But a variation during the orbital period is still present. Comparing the two depths emphasizes that the greater depth at the apocenters is a combination of the projection effect and the true broadening when the velocities become small near the apocenters.

4.2. The Amplitude of the Sagittarius Stream

We can also quantify the amplitude A of the stream fit from Section 3, defined as the number of RRab stars in the stream

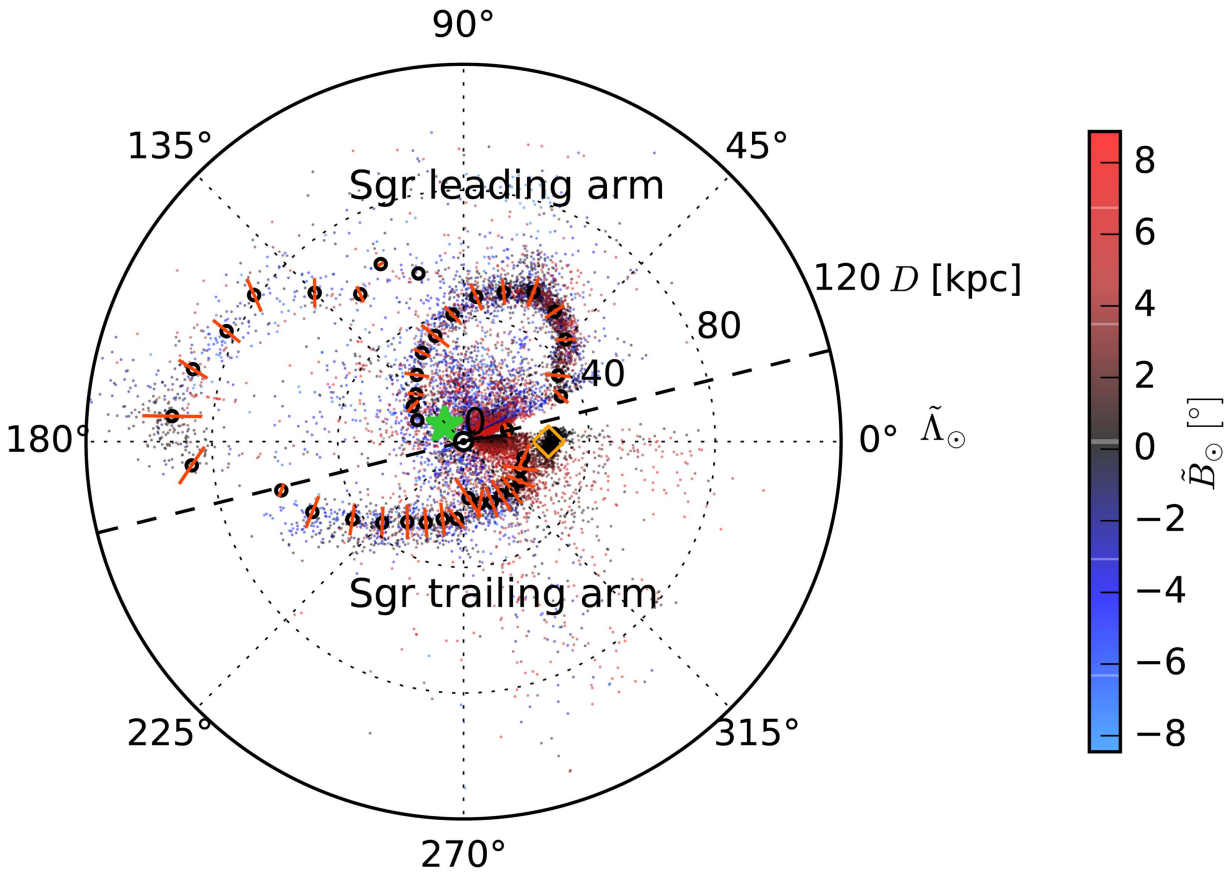

(a)

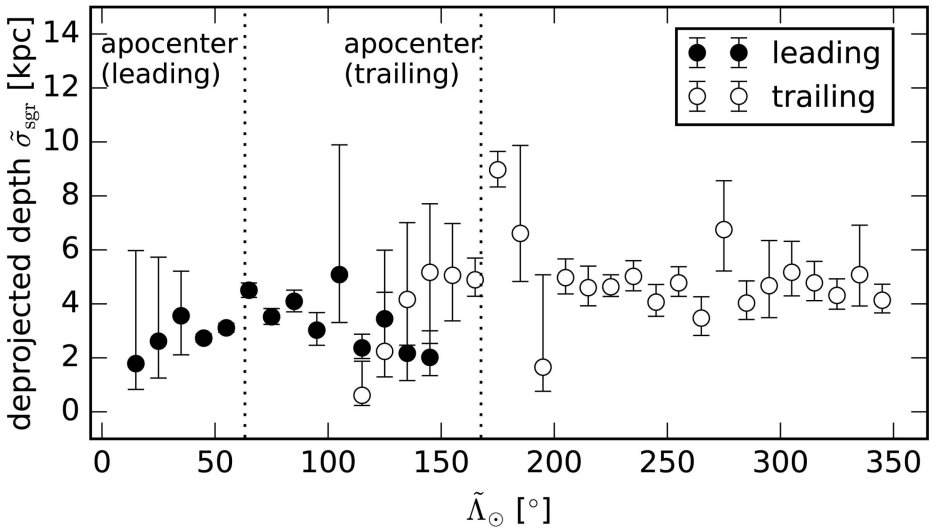

(b)

Figure 6. l.o.s. and deprojected depth of the Sgr stream. (a) Projection of the stream and its depth in cylindrical Sagittarius coordinates centered on the Sun. The orange bars indicate the deprojected depth, $\tilde{\sigma}_{\rm sgr}$. The source distance distribution is shown with the same data, symbols, and color coding as in Figure 4. (b) The deprojected depth $\tilde{\sigma}_{\rm sgr}$ of the Sagittarius stream from the RRab stars within $\pm 9°$ of the Sagittarius plane. Error bars indicate the range $D_{\rm sgr} \pm \delta D_{\rm sgr}$. The general trend in the depth, seen in Figure 5 for the l.o.s. depth $\sigma_{\rm sgr}$, is still present here, but the profile is flatter than the $\sigma_{\rm sgr}$ profile from Figure 5, because projection effects contribute to broadening near the apocenters. As in Figure 5, the apocenter positions are indicated as dashed lines. The deprojected depths along with their uncertainties are given in Tables 6 and 7 in the Appendix.

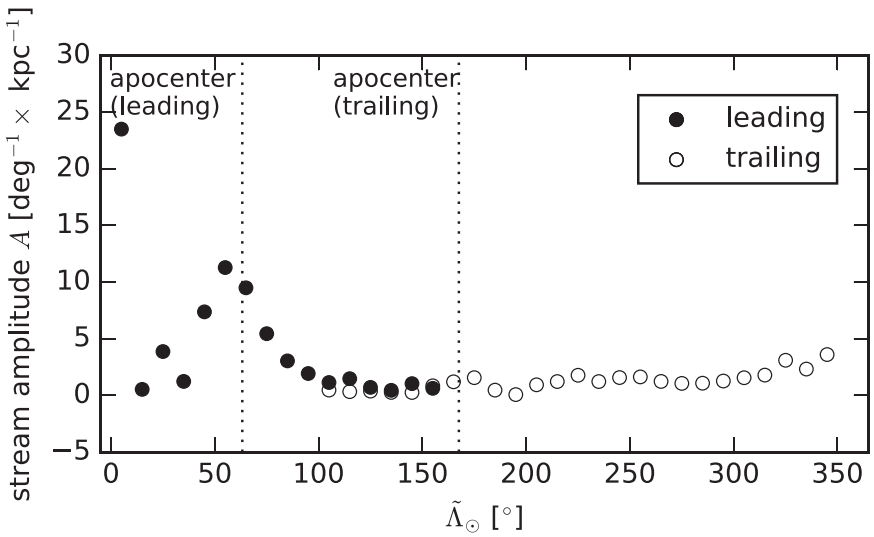

Figure 7. Amplitude of the stream, $A = (\#\text{sources within } \tilde{\Lambda}_\odot \pm \frac{\Delta\tilde{\Lambda}_\odot}{2}) \times f_{\rm sgr}/(\Delta\tilde{\Lambda}_\odot \times \sigma_{\rm sgr})$, for the $\tilde{\Lambda}_\odot$ bins. A shows an increase toward the apocenters, and is about six times larger near the leading arm's apocenter than near the trailing arm's. As in previous figures, the apocenter positions are indicated as dashed lines.

per degree as a function of $\tilde{\Lambda}_\odot$, i.e.,

$$A = \left(\#\text{sources within } \tilde{\Lambda}_\odot \pm \frac{\Delta\tilde{\Lambda}_\odot}{2}\right) \times f_{\rm sgr}/(\Delta\tilde{\Lambda}_\odot \times \sigma_{\rm sgr}). \tag{10}$$

The amplitudes for both the leading and trailing arms are given in Tables 8 and 9 in the Appendix.

Figure 7 shows the amplitudes plotted versus the $\tilde{\Lambda}_\odot$ bins. The value of A increases near the apocenter of the leading arm to about twice as much as away from its apocenter. Also near the apocenter of the trailing arm, A rises with respect to the value it has away from the apocenter, but not as strikingly as found for the leading arm. As the angular velocity decreases near the apocenter, we had expected to find an increased source density, and thus larger A, near the apocenters than in sections of the stream away from apocenters. In addition to this general statement, we find that the source density is about six times larger at the leading arm's apocenter than at the trailing arm's (compare also Figure 7 to Figure 4). We checked whether this can be partially explained by a selection effect, because the leading arm's apocenter has a smaller heliocentric distance than the trailing arm's. Using the selection function from Sesar et al. (2017c), we find that this falls far short of accounting for the difference in apocenter source densities between the leading and trailing arms, so incompleteness is not an issue here. Additionally, simulations like that of Dierickx & Loeb (2017) also show a similar behavior, see, e.g., their Figure 9, which shows a higher source density at the leading arm's apocenter.

4.3. The Apocenters and Orbital Precession of the Sagittarius Stream

Sources orbiting in a potential show a precession of their orbits, which means that they do not follow an identical orbit each time, but actually trace out a shape made up of rotated orbits. This is because the major axis of each orbit is rotating gradually within the orbital plane.

Orbits in the outer regions of galaxies with a spherically symmetric gravitational potential are expected to have a precession between 0° and 120° (Belokurov et al. 2014). Assuming a spherically symmetric potential, the precession depends primarily on the shape of the potential and thus on the radial mass distribution (Belokurov et al. 2014). Additionally it is also a function of the orbital energy and angular momentum distribution (Binney & Tremaine 2008).

The estimates of angular mean distance $D_{\rm sgr}$ of the Sgr stream that were obtained during this work enable us to make statements about the precession of the orbit. To do so, the angle between the leading and trailing apocenters is measured.

We calculate this angle by fitting a model to the distance data in both the leading and trailing arms, namely fitting a Gaussian and a (shifted and scaled) log-normal. A comparable fit was carried out by Belokurov et al. (2014). The models used here are unphysical, but can be applied here because they describe the angular distance distribution $D_{\rm sgr}(\tilde{\Lambda}_\odot)$ adequately in order to find the apocenters along with their uncertainties. As the angular distance distribution $D_{\rm sgr}(\tilde{\Lambda}_\odot)$ of the leading arm appears to be symmetrical with respect to the assumed apocenters, and also appears to be Gaussian-like, a Gaussian model is fitted to the $D_{\rm sgr}(\tilde{\Lambda}_\odot)$ of the leading arm. In contrast, the trailing arm shows a clear asymmetry. For this reason, we fit the trailing arm's distance distribution using a (shifted and scaled) log-normal, fitted for the range $105° \leqslant \tilde{\Lambda}_\odot \leqslant 265°$. With comparable results, a parabola can be fitted to the data.

The best-fit Gaussian model for the leading and trailing apocenters is shown in Figure 8. In this figure, blue and red lines show the best-fit Gaussian model for both the leading and trailing arms. The positions of the apocenters are each denoted by a circle symbol. Dashed lines mark the corresponding $\tilde{\Lambda}_\odot$ of each apocenter.

We find the leading apocenter at $\tilde{\Lambda}_\odot^L = 63\overset{\circ}{.}2 \pm 1\overset{\circ}{.}2$, reaching $D_{\rm sgr}^L = 50.88 \pm 0.45$ kpc, and the trailing apocenter at $\tilde{\Lambda}_\odot^T = 167\overset{\circ}{.}6 \pm 0\overset{\circ}{.}44$, reaching $D_{\rm sgr}^T = 91.12 \pm 0.09$ kpc.

For a more detailed discussion of the apocenter substructure, reaching up to 120 kpc from the Sun, we refer to Sesar et al. (2017c), Section 3.

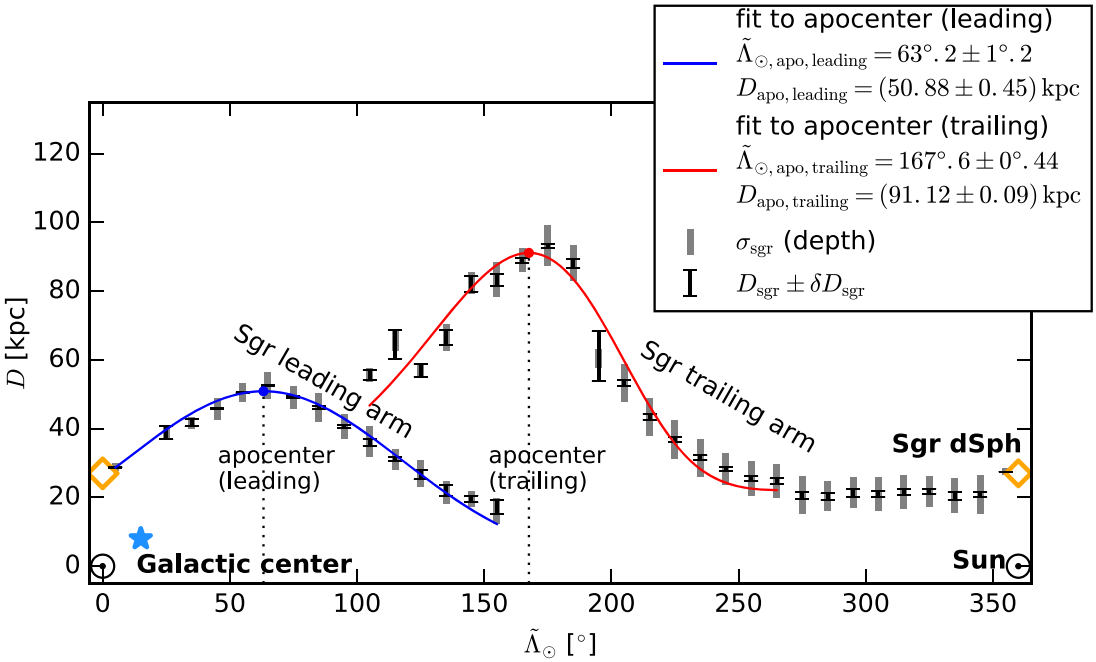

Figure 8. Apocenters of the Sgr stream by fitting $D_{\mathrm{sgr}}(\tilde{\Lambda}_\odot)$ with a Gaussian for the leading arm and a log-normal for the trailing arm. We derive the position of the leading apocenter as $\tilde{\Lambda}_\odot^L = 63\overset{\circ}{.}2 \pm 1\overset{\circ}{.}2$, reaching $D_{\mathrm{sgr}}^L = 50.88 \pm 0.45$ kpc, and that of the trailing apocenter as $\tilde{\Lambda}_\odot^T = 167\overset{\circ}{.}6 \pm 0\overset{\circ}{.}44$, reaching $D_{\mathrm{sgr}}^T = 91.12 \pm 0.09$ kpc. From this, we calculate the differential heliocentric orbital precession $\omega_\odot = \tilde{\Lambda}_\odot^T - \tilde{\Lambda}_\odot^L = 104\overset{\circ}{.}4 \pm 1\overset{\circ}{.}3$. The corresponding difference in heliocentric apocenter distances is 40.24 ± 0.45 kpc. Blue and red lines show the best-fit models for both the leading and trailing arms. The position of the apocenters is denoted by a circle symbol in the corresponding color. Dashed lines mark the corresponding $\tilde{\Lambda}_\odot$ of each apocenter.

The differential orbital precession $\omega_\odot = \tilde{\Lambda}_\odot^T - \tilde{\Lambda}_\odot^L$ is $104\overset{\circ}{.}4 \pm 1\overset{\circ}{.}3$, corresponding to a difference in heliocentric apocenter distances of 40.24 ± 0.45 kpc.

The actual Galactocentric orbital precession is slightly lower than the difference between the heliocentric apocenters. The Galactocentric distances and angles of the leading and trailing apocenters are calculated by taking into account that the Galactocentric distance of the Sun is 8 kpc. Consequently, the opening angle between the positions of the two apocenters, as viewed from the Galactic center, is then $\omega_{\mathrm{GC}} = 96\overset{\circ}{.}8 \pm 1\overset{\circ}{.}3$. The Galactocentric distance of the leading apocenter is then 47.8 ± 0.5 kpc, and that of the trailing apocenter 98.95 ± 1.3 kpc, resulting in a difference in mean Galactocentric apocenter distances of 47.45 ± 1.4 kpc.

4.4. Precession of the Orbital Plane of the Sagittarius Stream

Aside from the apocenter precession of the stream (see Section 4.3), the orbital plane itself might show a precession. To test this we obtain the weighted latitude of the stream RRab, $\langle \tilde{B}_\odot \rangle$, as a function of $\tilde{\Lambda}_\odot$. The weight of each star is the probability that the star is associated with the Sgr stream.

The fit as described in Section 3.1 was carried out for each bin i in $\tilde{\Lambda}_\odot$, resulting in a parameter set $\boldsymbol{\theta}_i = (f_{\mathrm{sgr},i}, D_{\mathrm{sgr},i}, \sigma_{\mathrm{sgr},i}, n_i)$ describing the stream and halo properties in the $\tilde{\Lambda}_\odot$ bin in each case.

We now again make use of the model for the observed heliocentric distances, Equation (1) with the halo described by Equation (3) and the stream described by Equation (4). We calculate $p_{\mathrm{sgr}}(l_j, b_j, D_j|\boldsymbol{\theta}_i)$ as the fraction of the likelihood that a star j is associated with the Sgr stream divided by the sum of the likelihood that it is associated with the Sgr stream and the likelihood that it is associated with the halo:

$$p_{\mathrm{sgr},j}(l_j, b_j, D_j|\boldsymbol{\theta}_i) = \frac{p_{\mathrm{stream}}(D|\boldsymbol{\theta}_i)}{(p_{\mathrm{halo}}(D|\boldsymbol{\theta}_i) + p_{\mathrm{stream}}(D|\boldsymbol{\theta}_i))}. \quad (11)$$

The weighted latitude $\langle \tilde{B}_\odot \rangle$ in a bin i is then calculated as

$$\langle \tilde{B}_\odot \rangle_i = \frac{\sum_j (\tilde{B}_{\odot,i} \times p_{\mathrm{sgr},j})}{\sum_j (p_{\mathrm{sgr},j})}. \quad (12)$$

We then use the difference in $\langle \tilde{B}_\odot \rangle$ for the leading and trailing arms to quantify the precession of the orbital plane.

The resulting $\langle \tilde{B}_\odot \rangle$ for both the leading and trailing arms are given in Tables 8 and 9 in the Appendix. Figure 9 shows $\langle \tilde{B}_\odot \rangle$ plotted versus the $\tilde{\Lambda}_\odot$ bins.

This gives evidence for the leading arm staying in or close to the plane defined by $\tilde{B}_\odot = 0^\circ$, whereas the trailing arm is found within within -5° to 5° around the plane. From this, we find a separation of $\sim 10^\circ$, as also derived by Law et al. (2005).

5. Discussion

We can now place our results in the context of existing work, and discuss the prospect of using them for dynamical stream modeling.

5.1. Comparison to the Model by Belokurov et al. (2014)

The best previous estimates of the heliocentric distances for a large part of the Sgr stream come from Belokurov et al. (2014), who used blue horizontal branch (BHB) stars, subgiant branch (SGB) stars, and red giant branch (RGB) stars from the Sloan Digital Sky Survey Data Release 8 (SDSS DR8). In Figure 10 we compare our heliocentric distances, $D_{\mathrm{sgr}} \pm \delta D_{\mathrm{sgr}}$, to those from Belokurov et al. (2014) (Figure 6 therein). We show the 1σ

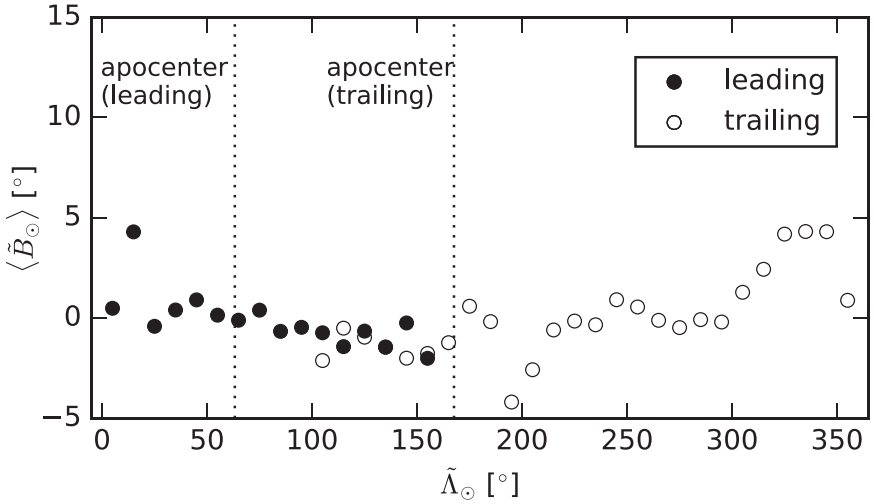

Figure 9. Weighted latitude of the stream RRab, $\langle \tilde{B}_\odot \rangle$, for the $\tilde{\Lambda}_\odot$ bins. The weight of each star is the probability that the star is associated with the Sgr stream, and $\langle \tilde{B}_\odot \rangle$ is then calculated from Equation (12). Except for $\tilde{\Lambda}_\odot = 15°$, the leading arm stays in or is close to the plane defined by $\tilde{B}_\odot = 0°$. In contrast, the trailing arm is found within $-5°$ to $5°$ around the plane. This results in a separation of $\sim 10°$, as also derived by Law et al. (2005).

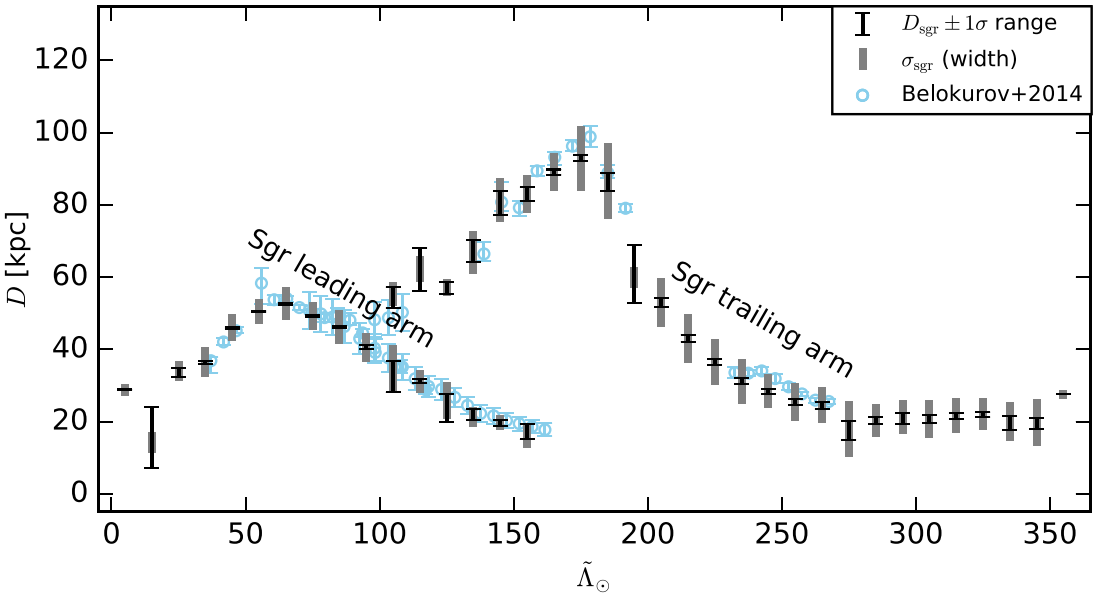

Figure 10. Comparison of the heliocentric distance estimates of the Sgr stream between this work and Belokurov et al. (2014). The $D_{\rm sgr}$, shown as black points together with their range $D_{\rm sgr} \pm \delta D_{\rm sgr}$ and estimated stream depth $\sigma_{\rm sgr}$ (gray bars), are compared with the estimates from Belokurov et al. (2014) (blue points), who traced parts of the Sgr stream, together with their uncertainties. The distances from Belokurov et al. (2014) show a slight trend toward larger values. Overall, the distance estimates are in good agreement. Uncertainties from our results are given as ranges $D_{\rm sgr} \pm \delta D_{\rm sgr}$; uncertainties from Belokurov et al. (2014) are given as their 1σ ranges if available, and assumed to be 10% if not stated otherwise.

uncertainties from Belokurov et al. (2014) where available, and assume the uncertainties to be 10% if not stated otherwise.

Overall, the two estimates are in good agreement, attesting to the quality of the analysis by Belokurov et al. (2014). The distances from Belokurov et al. (2014) may be systematically slightly larger; the fact that the RRab distances we use are directly tied to parallaxes from the *Hubble Space Telescope* (*HST*) and *Gaia* DR1 (Sesar et al. 2017a) should lend confidence to the distance scale of this work. Our new estimates for the mean distance are three times more precise, and presumably also accurate. The typical mean distance uncertainty in Belokurov et al. (2014) is 1–2 kpc and up to 0.1 $D_{\rm sgr}$ for most parts of the stream, whereas our work shows comparable or smaller $\delta D_{\rm sgr}$ (see Tables 4 and 5).

As mentioned before, our new map of the Sgr stream also has considerably more extensive angular coverage.

The high individual distance precision to the RRab of 3% allows us to map the l.o.s. depth of the stream, which Belokurov et al. (2014) could not do, or at least did not. For these reasons, our work improves the knowledge of the geometry of the Sgr stream significantly.

However, care must be taken in parts of the Sgr stream where the number of sources is comparatively low. The trailing arm's distance estimate for the bin centered on $\tilde{\Lambda}_\odot = 125°$ results from only 28 sources within the prior indicated by Figure 4(a), i.e., $D > 40$ kpc. In this bin, the estimated $D_{\rm sgr}$ is smaller than the $D_{\rm sgr}$ estimated for nearby bins, and the same applies for the estimated width of the stream, which appears to

be too narrow.

In both analyses, the apocenters of the leading and trailing arms are derived. We find the leading apocenter at $\tilde{\Lambda}_\odot^L = 63\overset{\circ}{.}2 \pm 1\overset{\circ}{.}2$, reaching $D_{\rm sgr}^L = 50.88 \pm 0.45$ kpc, and the trailing apocenter at $\tilde{\Lambda}_\odot^T = 167\overset{\circ}{.}6 \pm 0\overset{\circ}{.}44$, reaching $D_{\rm sgr}^T = 91.12 \pm 0.09$ kpc. The differential orbital precession $\omega_\odot = \tilde{\Lambda}_\odot^T - \tilde{\Lambda}_\odot^L$ is $104\overset{\circ}{.}4 \pm 1\overset{\circ}{.}3$, with a difference in heliocentric apocenter distances of 40.24 ± 0.45 kpc. Taking into account that the Galactocentric distance of the Sun is 8 kpc, the corresponding Galactocentric angle from our analysis is $\omega_{\rm GC} = 96\overset{\circ}{.}8 \pm 1\overset{\circ}{.}3$. The Galactocentric distance of the leading apocenter is then 47.8 ± 0.5 kpc, and that of the trailing apocenter 98.95 ± 1.3 kpc, resulting in a difference in mean Galactocentric apocenter distances of 47.45 ± 1.4 kpc.

If we assume that the trailing arm's apocenter is close to the maximum extent of the derived $D_{\rm sgr}$, as is done by fitting a Gaussian to the five closest points near the maximum extent, we find the trailing apocenter at $\tilde{\Lambda}_\odot^T = 173°4 \pm 2\overset{\circ}{.}0$, reaching $D_{\rm sgr}^T = 92.7 \pm 1.3$ kpc. The differential orbit precession $\omega_\odot = \tilde{\Lambda}_\odot^T - \tilde{\Lambda}_\odot^L$ is then $108\overset{\circ}{.}9 \pm 2\overset{\circ}{.}4$, with a difference in heliocentric apocenter distances of 41.82 ± 0.45 kpc. The Galactocentric angle is then slightly larger than for the log-normal fit, $\omega_{\rm GC} = 101\overset{\circ}{.}0 \pm 2\overset{\circ}{.}4$; the Galactocentric distance of the leading apocenter is 49.2 ± 0.5 kpc and that of the trailing apocenter is 100.7 ± 1.3 kpc, resulting in a difference in mean Galactocentric apocenter distances of 51.5 ± 1.4 kpc.

Belokurov et al. (2014) give the position of the leading apocenter as $\tilde{\Lambda}_\odot^L = 71\overset{\circ}{.}3 \pm 3\overset{\circ}{.}5$ with a Galactocentric distance $R^L = 47.8 \pm 0.5$ kpc, and the position of the trailing apocenter as $\tilde{\Lambda}_\odot^L = 170\overset{\circ}{.}5 \pm 1°$ with a Galactocentric distance $R^L = 102.5 \pm 2.5$ kpc. They state the derived Galactocentric orbital precession as $\omega = 93\overset{\circ}{.}2 \pm 3\overset{\circ}{.}5$.

To summarize the comparison:

1. Our analysis is done from one single survey and type of star, whereas the work by Belokurov et al. (2014) relies on BHB, SGB, and RGB stars. The extent and depth of PS1 3π enables us to provide a more extensive angular coverage of sources. This has resulted in the first complete (i.e., spanning $0° < \tilde{\Lambda}_\odot < 360°$) trace of the Sgr stream's heliocentric distance from a single type of star originating from a single survey.
2. The heliocentric mean distances of the stream from Belokurov et al. (2014) may be systematically slightly larger; the fact that the RRab distances we use are directly tied to *HST* and *Gaia* DR1 parallaxes (Sesar et al. 2017c) should lend confidence to the distance scale of this work.
3. Along with the extent of the Sgr stream, we can give its l.o.s. depth $\sigma_{\rm sgr}$, and deproject $\sigma_{\rm sgr}$ in order to get its true width.
4. Our analysis shows a Galactocentric orbital precession about 4° larger than measured by Belokurov et al. (2014), or 8° larger if assuming that the trailing arm's apocenter is close to the maximum extent of the derived $D_{\rm sgr}$. This is within the error range given by Belokurov et al. (2014). Generally speaking, the higher the Galactocentric orbital precession, the smoother the dark matter density is as a function of the Galactocentric radius. Logarithmic haloes should show an orbital precession of about 120° (Belokurov et al. 2014), whereas a smaller orbital precession angle indicates a profile with a sharper drop in the radial dark matter density (Belokurov et al. 2014). Finding this result, together with the result of Belokurov et al. (2014) as well as the simulation by Dierickx & Loeb (2017), is a strong indicator that a steeper profile than the logarithmic one should be considered for the dark matter halo of the Milky Way.

5.2. Bifurcation of the Leading Arm

Part of the Sgr stream's leading arm in the Galactic northern hemisphere is "bifurcated," or branched, in its projection on the sky (Belokurov et al. 2006). Starting at R.A. $\sim 190°$, the lower and upper declination branches of the stream, labeled A and B respectively (Belokurov et al. 2006), can be traced at least until R.A. $\sim 140°$. As stated by Fellhauer et al. (2006), the bifurcation likely arises from different stripping epochs, the young leading arm providing branch A and the old trailing arm branch B of the bifurcation. Belokurov et al. (2006) state that the SGB of branch B is significantly brighter and hence probably slightly closer than A, but the branch itself is reported to have much lower luminosity than A.

Their Figure 4 shows a noticeable, but small, difference in the distances estimated for branches A and B of 3–15 kpc, qualitatively consistent with the simulations by Fellhauer et al. (2006). However, Ruhland et al. (2011) found from an analysis of BHB stars in the stream that the branches differ by at most 2 kpc in distance. To follow up on this, we measured the RRab mean distances for small patches in both branches, as shown by the polygons in Figure 11, fitting a halo and stream model as described above in Section 3. This fitting led to the distance estimates as shown in Figure 11 and in Table 10 in the Appendix. Indeed a small difference in distance between the two branches can be found, branch B being closer than branch A, as in the simulation by Fellhauer et al. (2006). But the sparse sampling by the RR Lyrae makes this analysis inconclusive.

5.3. Bifurcation of the Trailing Arm

Analogous to the bifurcation of the leading arm found by Belokurov et al. (2006), Koposov et al. (2012) found a similar bifurcation in the trailing arm of the Sgr stream, consisting of two branches that are separated on the sky by $\sim 10°$.

This bifurcation was later confirmed and studied in greater detail by Slater et al. (2013), using MSTO and red clump (RC) stars from the Pan-STARRS1 survey, and by Navarrete et al. (2017), who have examined a large portion of approximately 65° of the Sgr trailing arm available in the imaging data from the VLT Survey Telescope (VST) ATLAS survey, using BHB and SGB stars, as well as RR Lyrae from the Catalina Real-Time Transient Survey.

They found the trailing arm appearing to be split along the l.o.s., with the additional stream component following a distinct distance track, and a difference in heliocentric distances exists of ~ 5 kpc. The bulk of the "bright stream" (Slater et al. 2013) is below the Sgr orbital plane (thus $\tilde{B}_\odot < 0°$), while the "faint stream" lies mostly above the plane ($\tilde{B}_\odot > 0°$).

We compare here our distance distributions to the findings of Slater et al. (2013) and Navarrete et al. (2017) for different regions in ($\tilde{\Lambda}_\odot$, $\tilde{B}_\odot$).

Navarrete et al. (2017) report a bifurcation in the ($\tilde{\Lambda}_\odot$, $\tilde{B}_\odot$) plane with a separation of $\sim 10°$. Likely due to our relatively sparse source density, we cannot find an indicator for a bifurcation in the ($\tilde{\Lambda}_\odot$, $\tilde{B}_\odot$) plane that would lead to a "bright stream" and a "faint stream."

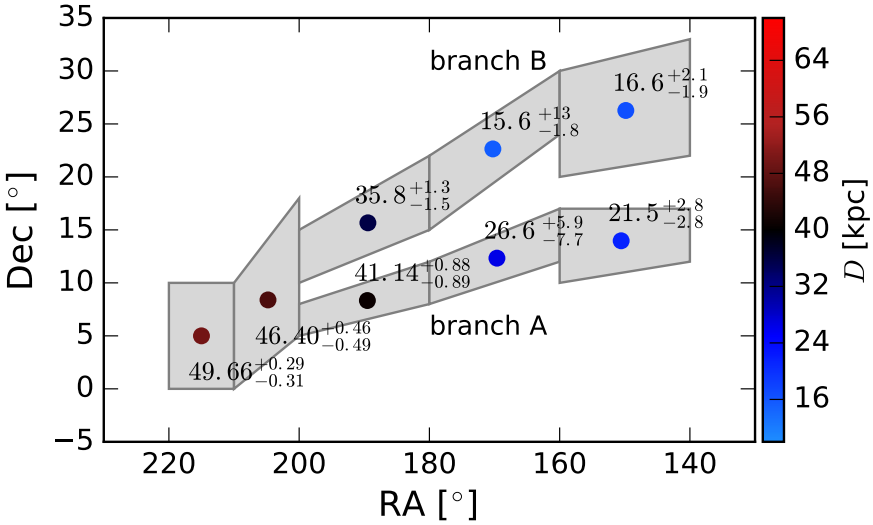

Figure 11. Heliocentric distance estimates for patches covering branches A and B of the Sagittarius stream in equatorial coordinates. For each patch, the fit using the halo and stream model as described above in Section 3 was carried out to derive distance estimates. The points set at the centroid of each polygon indicate the heliocentric distance D in kiloparsecs as estimated from the sample within each polygon. The range $D_{\rm sgr} \pm \delta D_{\rm sgr}$ is indicated.

We then checked whether we can identify l.o.s. substructures, and made histograms of the heliocentric distance distribution for several patches along the trailing arm of the Sgr stream.

In Figure 12, we give a histogram of our distance estimates in one of the regions probed by Navarrete et al. (2017) and Slater et al. (2013). This specific region was also probed using RR Lyrae by Navarrete et al. (2017) (see their Figure 9). We give our estimates of the heliocentric distance D and the distance modulus $m - M$ (Sesar et al. 2017c). Blue markers represent substructures found by Navarrete et al. (2017). A similar shape of the distance distribution is found, and we also detect the substructures they call "SGB 1" and "SGB 2." We find "SGB 1" at a slightly larger distance than Navarrete et al. (2017). We find "SGB 2" split into two components.

We were also able to identify similar substructures to those found by Navarrete et al. (2017) and Slater et al. (2013) within other patches of the trailing arm of the Sgr stream, and count them as tentative but marginally significant because of the relatively low density of our tracers.

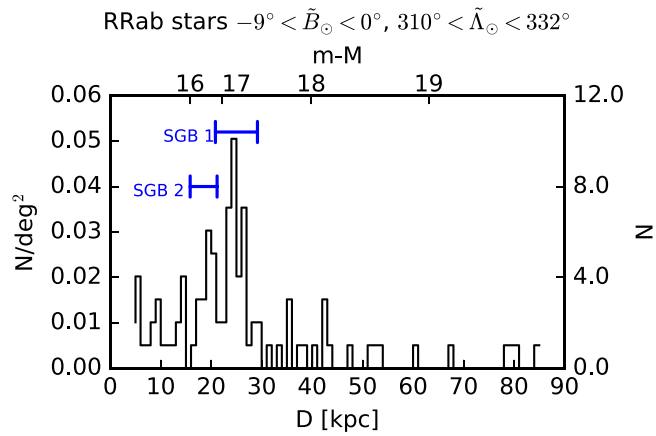

Figure 12. Heliocentric distance distribution for RRab stars in the trailing tail. Analogous to the bifurcation of the leading arm found by Belokurov et al. (2006), Slater et al. (2013) and Navarrete et al. (2017) report a similar bifurcation in the trailing tail. We compare our distance distributions to the findings of Slater et al. (2013) and Navarrete et al. (2017) for different regions in ($\tilde{B}_\odot$, $\tilde{\Lambda}_\odot$). This plot gives our distance estimates in a region also probed using RR Lyrae by Navarrete et al. (2017) (see their Figure 9). We give our estimates of the heliocentric distance D and the distance modulus $m - M$ (Sesar et al. 2017c). Blue markers represent substructures found by Navarrete et al. (2017).

6. Summary

In this work, we quantified the geometry of the Sagittarius stream, approximating the l.o.s. density of the Sagittarius stream by a Gaussian distribution centered on the distance $D_{\rm sgr}$ with l.o.s. depth $\sigma_{\rm sgr}$. This model was used to estimate the distance and depth of the Sgr stream as given by RR Lyrae candidates (RRab with completeness $\geqslant 0.8$, purity $= 0.9$ up to 80 kpc, distance precision of 3%) resulting from the classification that incorporates fitting of the period.

The fitting resulted in the best and first basically complete (i.e., spanning $0° < \tilde{\Lambda}_\odot < 360°$) trace of the Sgr stream's heliocentric distance as well as l.o.s. depth. This model further allows one to measure many properties of the Sgr stream. We have measured the depth $\sigma_{\rm sgr}$ as well as the deprojected depth of the stream. The function of $\sigma_{\rm sgr}$ versus $\tilde{\Lambda}_\odot$ can be partially explained by projection effects, and partially by projection effects due to the angle our l.o.s. direction forms with the stream direction. Deprojection removes the l.o.s. effects and thus results in a depth of the stream that will be very helpful when comparing simulations to observational data. Furthermore, we computed the amplitude of the Sgr stream as the number of RRab stars in the stream per degree as a function of its longitude $\tilde{\Lambda}_\odot$. The fit allows us to precisely determine the apocenter positions, from which we then calculate the orbital precession. We also find a strong indicator for a precession of the orbital plane. We have measured the Galactocentric angle between the apocenters of the leading and trailing arms of the Sgr stream and the difference between their respective distances.

We now have a model of the geometry of the Sgr stream at hand that can be used to further constrain the Milky Way's potential.

N.H., B.S., and H.-W.R. acknowledge funding from the European Research Council under the European Union's Seventh Framework Programme (FP 7) ERC Grant Agreement n. [321035].

The Pan-STARRS1 Surveys (PS1) have been made possible through contributions of the Institute for Astronomy, the University of Hawaii, the Pan-STARRS Project Office, the Max-Planck Society and its participating institutes, the Max

Planck Institute for Astronomy, Heidelberg and the Max Planck Institute for Extraterrestrial Physics, Garching, The Johns Hopkins University, Durham University, the University of Edinburgh, Queen's University Belfast, the Harvard-Smithsonian Center for Astrophysics, the Las Cumbres Observatory Global Telescope Network Incorporated, the National Central University of Taiwan, the Space Telescope Science Institute, the National Aeronautics and Space Administration under Grant No. NNX08AR22G issued through the Planetary Science Division of the NASA Science Mission Directorate, the National Science Foundation under Grant No. AST-1238877, the University of Maryland, and Eotvos Lorand University (ELTE) and the Los Alamos National Laboratory.

Appendix
Tables

Table 1 gives the PS1 RRab stars with $|\tilde{B}_{\odot}| < -9°$ that this analysis is based on.

Tables 2 and 3 give the minimum and maximum priors on $D_{\rm sgr}$, $D_{\rm minprior}$ and $D_{\rm maxprior}$, as indicated in Figure 4. The annotation "max" within the tables state that the given value is the maximum observed heliocentric distance D in the given $\tilde{\Lambda}_{\odot}$ interval.

Tables 4 and 5 give the geometry of the Sagittarius stream, represented by its extent and depth as inferred from the analysis presented in this paper.

Tables 6 and 7 give the deprojected depth of the Sagittarius stream.

Tables 8 and 9 give the amplitude of the Sagittarius stream, as well as its weighted latitude $\langle \tilde{B}_{\odot} \rangle$, as calculated by Equation (12).

Table 10 gives the distance estimates for branches A and B of the Sagittarius stream.

Table 1
PS1 RRab Stars with $|\tilde{B}_{\odot}| < -9°$

R.A. (deg)	Decl. (deg)	score$_{3,\rm ab}$[a]	DM[b] (mag)	Period (day)	ϕ_0[c] (day)	A_r[d] (mag)
181.40332	7.77677	1.00	17.08	0.6752982619	0.24526	0.75
181.12043	8.28025	0.91	12.79	0.5382632283	0.44801	0.63
180.08748	9.10501	1.00	17.76	0.5203340425	−0.46188	0.88

Notes.
[a] Final RRab classification score.
[b] Distance modulus. The uncertainty in distance modulus is 0.06(rnd) ± 0.03(sys) mag.
[c] Phase offset (see Equation (2) of Sesar et al. 2017c).
[d] PS1 r-band light-curve amplitude.

(This table is available in its entirety in machine-readable form.)

Table 2
$D_{\rm sgr}$ Prior, Leading Arm

$\tilde{\Lambda}_{\odot}$ Interval (deg)	$D_{\rm minprior}$ (kpc)	$D_{\rm maxprior}$ (kpc)
[10, 20[	5	27.3 (max)
[20, 30[	30	35
[30, 40[	30	37
[40, 50[	10	77.5 (max)
[50, 60[	10	110.1 (max)
[60, 70[	10	98.9 (max)
[70, 80[	10	97.2 (max)
[80, 90[	20	70
[90, 100[	20	60
[100, 110[	25	50
[110, 120[	20	50
[120, 130[	15	40
[130, 140[	20	40
[140, 150[	15	40
[150, 160[	15	40

Table 3
$D_{\rm sgr}$ Prior, Trailing Arm

$\tilde{\Lambda}_{\odot}$ Interval (deg)	$D_{\rm minprior}$ (kpc)	$D_{\rm maxprior}$ (kpc)
[100, 110[	50	95.1 (max)
[110, 120[	50	98.9 (max)
[120, 130[	40	92.6 (max)
[130, 140[	10	92.7 (max)
[140, 150[	40	106.0 (max)
[150, 160[	40	134.2 (max)
[160, 170[	10	125.1 (max)
[170, 180[	10	131.7 (max)
[180, 190[	10	103.6 (max)
[190, 200[	10	72.6 (max)
[200, 210[	40	73.8 (max)
[210, 220[	10	64.6 (max)
[220, 230[	30	60
[230, 240[	30	60
[240, 250[	20	50
[250, 260[	10	40
[260, 270[	10	50
[270, 280[	10	50
[280, 290[	10	50
[290, 300[	10	50
[300, 310[	10	50
[310, 320[	10	80.0 (max)
[320, 330[	10	84.7 (max)
[330, 340[	10	64.6 (max)
[340, 350[	10	86.4 (max)
[350, 360[	10	50.0

Table 4
Fitted Parameters for Sagittarius Stream, Leading Arm

$\tilde{\Lambda}_\odot$ (deg)	$f_{\rm sgr}$ [a]	$D_{\rm sgr}$ (kpc)[b]	$\delta_-(D_{\rm sgr})$	$\delta_+(D_{\rm sgr})$	$2\delta_-(D_{\rm sgr})$	$2\delta_+(D_{\rm sgr})$	$\sigma_{\rm sgr}$ (kpc)[c]	$\delta_-(\sigma_{\rm sgr})$	$\delta_+(D_{\rm sgr})$	$2\delta_-(\sigma_{\rm sgr})$	$2\delta_+(\sigma_{\rm sgr})$
5	0.18	28.830	0.10	0.094	0.20	0.18	1.621	0.079	0.091	0.15	0.18
15	0.052	14.3	7.1	9.7	9.1	12.0	2.8	1.5	6.5	1.7	15
25	0.050	34.14	1.8	0.66	3.8	0.83	2.8	1.4	3.3	1.7	9.3
35	0.051	36.65	0.60	0.27	1.9	0.34	4.1	1.7	1.9	2.9	4.6
45	0.38	45.94	0.24	0.25	0.48	0.52	3.68	0.19	0.20	0.36	0.43
55	0.51	50.50	0.17	0.17	0.34	0.33	3.33	0.18	0.18	0.34	0.38
65	0.61	52.59	0.21	0.21	0.43	0.44	4.52	0.27	0.27	0.54	0.53
75	0.41	49.19	0.26	0.27	0.52	0.53	3.75	0.30	0.33	0.57	0.72
85	0.36	46.22	0.40	0.39	0.83	0.78	4.66	0.44	0.47	0.79	0.99
95	0.21	40.59	0.48	0.53	0.95	1.1	3.88	0.72	0.83	1.3	1.9
105	0.26	34.8	6.7	1.9	9.4	2.8	6.3	2.2	6.0	3.2	8.8
115	0.22	31.19	0.57	0.54	1.3	1.0	3.08	0.51	0.66	0.91	1.7
125	0.25	25.9	5.9	1.9	9.9	3.0	5.0	1.9	3.7	2.8	6.2
135	0.067	21.34	0.92	2.1	1.3	8.9	2.7	1.3	2.7	1.7	6.5
145	0.13	19.66	0.87	0.80	2.2	20.0	2.05	0.68	1.0	0.99	2.5
155	0.15	16.2	1.1	3.2	1.1	3.2	3.4	2.2	2.6	2.2	2.6

Notes.
[a] Fraction of sources in the Sgr stream.
[b] Mean heliocentric distance of the Sgr stream.
[c] Line-of-sight depth of the Sgr stream.

Table 5
Fitted Parameters for Sagittarius Stream, Trailing Arm

$\tilde{\Lambda}_\odot$ (deg)	$f_{\rm sgr}$ [a]	$D_{\rm sgr}$ (kpc)[b]	$\delta_-(D_{\rm sgr})$	$\delta_+(D_{\rm sgr})$	$2\delta_-(D_{\rm sgr})$	$2\delta_+(D_{\rm sgr})$	$\sigma_{\rm sgr}$ (kpc)[c]	$\delta_-(\sigma_{\rm sgr})$	$\delta_+(D_{\rm sgr})$	$2\delta_-(\sigma_{\rm sgr})$	$2\delta_+(\sigma_{\rm sgr})$
105	0.055	55.4	3.9	1.9	5.2	3.5	3.2	1.5	7.2	2.0	13
115	0.056	62.3	6.0	5.8	11	10	3.5	2.2	7.3	2.5	14
125	0.059	57.2	1.9	1.4	11	11	2.3	0.97	2.2	1.3	12
135	0.084	66.9	2.6	3.2	5.0	7.2	5.8	2.4	4.0	4.1	9.9
145	0.095	81.3	4.1	2.7	8.7	4.4	6.1	3.1	3.0	4.6	6.2
155	0.31	83.1	1.9	1.8	1.9	1.8	5.2	1.7	3.0	1.7	2.0
165	0.36	89.02	0.72	0.74	1.5	1.5	5.13	0.64	0.85	1.2	2.0
175	0.63	92.98	0.79	0.81	1.6	1.6	8.99	0.64	0.68	1.3	1.4
185	0.40	86.7	3.0	2.2	7.0	4.6	10.5	2.8	5.2	4.6	8.7
195	0.082	60.0	7.1	9.0	17	12	2.8	1.5	5.8	1.8	15
205	0.55	53.0	1.2	1.1	2.6	2.1	6.78	0.82	0.95	1.5	2.2
215	0.61	43.15	1.1	0.88	2.4	1.8	6.65	0.97	1.2	1.8	2.4
225	0.71	36.55	0.87	0.75	1.8	1.4	6.28	0.49	0.61	0.97	1.4
235	0.55	31.17	0.70	0.80	1.1	1.6	6.16	0.65	0.71	1.3	1.5
245	0.58	28.41	0.85	0.69	1.9	1.3	4.66	0.60	0.75	1.1	1.7
255	0.62	25.57	0.85	0.72	1.9	1.4	5.14	0.54	0.64	1.0	1.4
265	0.43	24.7	1.2	0.87	2.8	1.6	4.86	0.90	1.1	1.7	2.4
275	0.60	18.0	3.1	2.1	7.0	3.9	7.7	1.8	2.1	3.3	4.2
285	0.32	20.34	1.1	0.83	2.7	1.6	4.44	0.67	0.90	1.2	2.2
295	0.27	21.2	1.8	1.2	5.4	2.2	4.7	1.2	1.7	2.0	4.2
305	0.37	20.8	1.3	1.0	3.4	1.9	5.17	0.88	1.1	1.6	2.8
315	0.45	21.66	0.95	0.80	2.0	1.5	4.84	0.67	0.80	1.3	1.8
325	0.48	22.00	0.75	0.62	1.7	1.2	4.41	0.52	0.63	0.97	1.5
335	0.40	20.1	2.3	1.4	7.3	2.3	5.3	1.2	1.9	2.1	4.6
345	0.47	19.7	1.7	1.3	4.7	2.4	6.43	0.73	0.92	1.4	2.3
355	0.43	27.605	0.054	0.053	0.11	0.11	1.245	0.048	0.047	0.091	0.096

Notes.
[a] Fraction of sources in the Sgr stream.
[b] Mean heliocentric distance of the Sgr stream.
[c] Line-of-sight depth of the Sgr stream.

Table 6
Deprojected Depth $\tilde{\sigma}_{\rm sgr}$ for the Sagittarius Stream (see Section 4.1), Leading Arm

$\tilde{\Lambda}_\odot$ (deg)	$\tilde{\sigma}_{\rm sgr}$	$\delta_-(\tilde{\sigma}_{\rm sgr})$	$\delta_+\tilde{\sigma}_{\rm sgr}$
15	1.79	0.83	6.0
25	2.6	1.3	5.7
35	3.6	2.1	5.2
45	2.7	2.6	2.9
55	3.1	2.9	3.3
65	4.5	4.2	4.8
75	3.5	3.2	3.8
85	4.1	3.7	4.5
95	3.0	2.5	3.7
105	5.1	3.3	9.9
115	2.4	2.0	2.9
125	3.4	2.2	6.0
135	2.2	1.2	4.3
145	1.7	1.2	2.6

Table 7
Deprojected Depth $\tilde{\sigma}_{\rm sgr}$ for the Sagittarius Stream (see Section 4.1), Trailing Arm

$\tilde{\Lambda}_\odot$ (deg)	$\tilde{\sigma}_{\rm sgr}$	$\delta_-(\tilde{\sigma}_{\rm sgr})$	$\delta_+\tilde{\sigma}_{\rm sgr}$
115	0.61	0.24	1.9
125	2.2	1.3	4.4
135	4.2	2.5	7.0
145	5.2	2.5	7.7
155	5.1	3.4	7.0
165	4.9	4.3	5.7
175	9.0	8.3	9.6
185	6.6	4.8	9.9
195	1.65	0.76	5.1
205	5.0	4.4	5.7
215	4.6	3.9	5.4
225	4.6	4.3	5.1
235	5.0	4.5	5.6
245	4.1	3.5	4.7
255	4.8	4.3	5.4
265	3.5	2.8	4.3
275	6.8	5.2	8.6
285	4.0	3.4	4.9
295	4.7	3.5	6.3
305	5.2	4.3	6.3
315	4.8	4.1	5.6
325	4.3	3.8	4.9
335	5.1	3.9	6.9
345	4.1	3.7	4.7

Table 8
Amplitude A (see Section 4.2) and Weighted Latitude $\langle\tilde{B}_\odot\rangle$ (see Section 4.4) for the Sagittarius Stream, Leading Arm

$\tilde{\Lambda}_\odot$ (deg)	A (deg^{-1} kpc^{-1})	$\langle\tilde{B}_\odot\rangle$ (deg)
5	24	0.48
15	0.53	4.3
25	3.9	−0.41
35	1.2	0.40
45	7.4	0.90
55	11	0.14
65	9.5	−0.11
75	5.4	0.39
85	3.0	−0.67
95	1.9	−0.47
105	1.1	−0.74
115	1.5	−1.4
125	0.70	−0.65
135	0.44	−1.4
145	1.0	−0.25
155	0.62	−2.0

Table 9
Amplitude A (see Section 4.2) and weighted latitude $\langle\tilde{B}_\odot\rangle$ (see Section 4.4) for the Sagittarius Stream, Trailing Arm

$\tilde{\Lambda}_\odot$ (deg)	A (deg^{-1} kpc^{-1})	$\langle\tilde{B}_\odot\rangle$ (deg)
105	0.47	−2.1
115	0.33	−0.51
125	0.37	−0.96
135	0.26	−1.5
145	0.25	−2.0
155	0.85	−1.8
165	1.2	−1.2
175	1.6	0.59
185	0.46	−0.18
195	0.067	−4.2
205	0.93	−2.6
215	1.2	−0.60
225	1.8	−0.15
235	1.2	−0.34
245	1.6	0.91
255	1.6	0.55
265	1.2	−0.12
275	1.1	−0.48
285	1.1	−0.08
295	1.3	−0.20
305	1.6	1.3
315	1.8	2.4
325	3.1	4.2
335	2.3	4.3
345	3.6	4.3
355	54	0.88

Table 10
Possible Bifurcation in the Sagittarius Stream

R. A. (deg)[a]	Decl. (deg)[a]	f_{sgr} [b]	D_{sgr} (kpc)[c]	$\delta_-(D_{sgr})$	$\delta_+(D_{sgr})$	$2\sigma\delta_-(D_{sgr})$	$2\sigma\delta_+(D_{sgr})$	σ_{sgr} (kpc)[d]	$\delta_-(\sigma_{sgr})$	$\delta_+(\sigma_{sgr})$	$2\sigma\delta_-(\sigma_{sgr})$	$2\sigma\delta_+(\sigma_{sgr})$
215	5	0.49	49.77	0.31	0.32	0.63	0.66	3.18	0.43	0.52	0.83	1.1
204.783	8.391	0.41	46.37	0.51	0.49	1.0	0.94	4.56	0.52	0.57	1.0	1.2
189.524	8.333	0.32	41.22	1.1	0.87	2.8	1.7	5.48	1.0	1.3	1.9	3.3
189.444	15.667	0.44	20.0	6.0	6.6	9.1	15	16.14	3.5	2.5	8.9	3.6
169.63	12.333	0.40	21.7	7.8	6.5	11	12	12.0	4.2	4.3	8.7	6.8
170.256	22.641	0.33	17	5.8	12	7.4	13	10.1	7.4	2.6	8.7	4.5
150.556	13.972	0.15	25.18	1.4	0.96	4.5	1.7	2.0	0.72	1.4	0.99	4.2
149.841	26.27	0.11	19.46	4.3	1.4	8.7	50	2.9	1.5	4.0	1.9	10

Notes.
[a] For each polygon, the centroid of its (α, δ) is given, as used in Figure 11.
[b] Fraction of sources in the Sgr stream.
[c] Mean heliocentric distance of the Sgr stream.
[d] Line-of-sight depth of the Sgr stream.

ORCID iDs

Nina Hernitschek https://orcid.org/0000-0003-1681-0430
Branimir Sesar https://orcid.org/0000-0002-0834-3978
Hans-Walter Rix https://orcid.org/0000-0003-4996-9069
David Martinez-Delgado https://orcid.org/0000-0003-3835-2231
Nicolas F. Martin https://orcid.org/0000-0002-1349-202X
Nick Kaiser https://orcid.org/0000-0001-6511-4306
Klaus Hodapp https://orcid.org/0000-0003-0786-2140
Kenneth C. Chambers https://orcid.org/0000-0001-6965-7789
Richard Wainscoat https://orcid.org/0000-0002-1341-0952
Eugene Magnier https://orcid.org/0000-0002-7965-2815
Nigel Metcalfe https://orcid.org/0000-0001-9034-4402
Peter W. Draper https://orcid.org/0000-0002-7204-9802

References

Belokurov, V., Koposov, S. E., & Evans, N. W. 2014, MNRAS, 437, 116
Belokurov, V., Zucker, D. B., Evans, N. W., et al. 2006, ApJL, 642, L137
Binney, J., & Tremaine, S. 2008, Galactic Dynamics (2nd ed.; Princeton, NJ: Princeton Univ. Press)
Bovy, J., Bahmanyar, A., Fritz, T. K., et al. 2016, ApJ, 883, 31
Chambers, K. C., Magnier, E. A., Metcalfe, N., et al. 2016, arXiv:1612.05560
Dierickx, M. I. P., & Loeb, A. 2017, ApJ, 836, 92
Drake, A. J., Catelan, M., Djorgovski, S. G., et al. 2013, ApJ, 765, 154
Drake, A. J., Graham, M. J., Djorgovski, S. G., et al. 2014, ApJS, 213, 9
Duffau, S., Vivas, A. K., Zinn, R., et al. 2014, A&A, 566, A118
Eyre, A., & Binney, J. 2009, MNRAS, 400, 548
Fardal, M. A., Huang, S., & Weinberg, M. D. 2015, MNRAS, 452, 301
Fellhauer, M., Belokurov, V., Evans, N. W., et al. 2006, ApJ, 651, 167
Foreman-Mackey, D., Hogg, D. W., Lang, D., et al. 2013, PASP, 125, 925
Gaia Collaboration, Prusti, T., de Bruijne, J. H. J., et al. 2016, A&A, 595, A1
Gibbons, S. L. J., Belokurov, V., & Evans, N. W. 2014, MNRAS, 445, 3788
Goodman, J., & Weare, J. 2010, Comm. App. Math. Comp. Sci., 5, https://msp.org/camcos/2010/5-1/p04.xhtml
Helmi, A. 2004a, MNRAS, 351, 643
Helmi, A. 2004b, ApJL, 610, L97
Hernitschek, N., Rix., H.-W., Schlafly, E. F., et al. 2016, ApJ, 817, 73
Ibata, R., & Lewis, G. F. 1998, ApJ, 500, 575
Ibata, R. A., Gilmore, G., & Irwin, M. J. 1994, Natur, 370, 194
Johnston, K. V., Spergel, D. N., & Hernquist, L. 1995, ApJ, 451, 598
Jurić, M., Ivezić, Ž, Brooks, A., et al. 2008, ApJ, 673, 864
Kaiser, N., Burgett, W, Chambers, K, et al. 2010, Proc. SPIE, 7703, 77330E
Karachentsev, I. D., Karachentseva, V. E., Huchtmeier, W. K., et al. 2004, AJ, 127, 2031
Koposov, S. E., Belokurov, V., Evans, N. E., et al. 2012, ApJ, 750, 80
Koposov, S. E., Rix, H. W., Hogg, D. W., et al. 2010, ApJ, 712, 260
Law, D. R., Johnston, K. V., & Majewski, S. R. 2005, ApJ, 619, 800
Law, D. R., & Majewski, S. R. 2005, ApJ, 619, 807
Law, D. R., & Majewski, S. R. 2010, ApJ, 714, 229
Majewski, S. R., Skrutskie, M. F., Weinberg, M. D., & Ostheimer, J. C. 2003, ApJ, 599, 1082
Martínez-Delgado, D., Aparicio, A., Gómez-Flechoso, M. A., Carrera, R., et al. 2001, ApJL, 549, L199
Martínez-Delgado, D., Gómez-Flechoso, M. Á., Aparicio, A., Carrera, R., et al. 2003, ApJ, 601, 242
Mateo, M., Olszewski, E. W., & Morrison, H. L. 1998, ApJL, 508, L55
Navarrete, C., Belokurov, V., Koposov, E. E., et al. 2017, MNRAS, 467, 1329
Newberg, H. J., Willett, B. A., Yanny, B., et al. 2010, ApJ, 771, 32
Newberg, H. J., Yanny, B., Grebel, E. K., et al. 2003, ApJL, 596, L191
Newberg, H. J., Yanny, B., & Willet, B. A. 2009, ApJL, 700, L61
Niederste-Ostholt, M., Belokurov, V., Evans, N. W., et al. 2010, ApJ, 712, 516
Peñarrubia, J., Belokurov, V., Evans, N. W., et al. 2010, MNRAS, 408, L26
Ruhland, C., Bell, E. F., Rix, H.-W., & Xue, X.-X. 2011, ApJ, 731, 119
Sanders, J. L., & Binney, J. 2013, MNRAS, 433, 1826
Sesar, B., Bovy, J., Bernard, E. J., et al. 2016, ApJ, 809, 59
Sesar, B., Cohen, J. G., Levitan, D., et al. 2012, ApJ, 755, 134
Sesar, B., Fouesneau, M., Price-Whelan, A. M., et al. 2017a, ApJ, 838, 107
Sesar, B., Hernitschek, N., Dierickx, M. I. P., Fardal, M. A., & Rix, H.-W. 2017b, ApJL, 844, L4
Sesar, B., Hernitschek, N., Mitrović, S., et al. 2017c, AJ, 153, 204
Sesar, B., Ivezić, Ž, Scott, J. S., et al. 2013, AJ, 146, 21
Slater, C. T., Bell, E. F., Schlafly, E. F., et al. 2013, ApJ, 762, 6
Stubbs, C. W., Doherty, P., Cramer, C., et al. 2010, ApJS, 191, 376
Tonry, J.L, Stubbs, C. W., Lykke, K. R., et al. 2012, ApJ, 750, 99
Vivas, A. K., Jaffél, Y. L., Zinn, R., et al. 2008, ApJ, 136, 1645
Vivas, A. K., Zinn, R., Abadl, C., et al. 2004, ApJ, 127, 1158
Vivas, A. K., Zinn, R., Andrews, P., et al. 2001, ApJL, 554, L33
Zinn, R., Horowitz, B., Vivas, A. K., et al. 2014, ApJ, 781, 22